The Astrophysical Journal, 975:214 (16pp), 2024 November 10 https://doi.org/10.3847/1538-4357/ad7d09

No Redshift Evolution in the Fe II/Mg II Flux Ratios of Quasars across Cosmic Time

Danyang Jiang[1,2], Masafusa Onoue[2,3,4,19], Linhua Jiang[1,2], Samuel Lai[5], Eduardo Bañados[6], George D. Becker[7], Manuela Bischetti[8], Sarah E. I. Bosman[6,9], Rebecca L. Davies[10,11], Valentina D'Odorico[12,13,14], Emanuele Paolo Farina[15], Martin G. Haehnelt[16], Chiara Mazzucchelli[17], Jan-Torge Schindler[18], Fabian Walter[6], and Yongda Zhu[7]

[1] Department of Astronomy, School of Physics, Peking University, Beijing 100871, People's Republic of China
[2] Kavli Institute for Astronomy and Astrophysics, Peking University, Beijing 100871, People's Republic of China
[3] Kavli Institute for the Physics and Mathematics of the Universe (Kavli IPMU, WPI), The University of Tokyo Institutes for Advanced Study, The University of Tokyo, Kashiwa, Chiba 277-8583, Japan
[4] Center for Data-Driven Discovery, Kavli IPMU (WPI), UTIAS, The University of Tokyo, Kashiwa, Chiba 277-8583, Japan
[5] Research School of Astronomy and Astrophysics, Australian National University, Canberra, ACT 2611, Australia
[6] Max Planck Institut für Astronomie, Königstuhl 17, D-69117, Heidelberg, Germany
[7] Department of Physics and Astronomy, University of California, Riverside, CA 92521, USA
[8] Dipartimento di Fisica, Sezione di Astronomia, Universitá di Trieste, via Tiepolo 11, I-34143 Trieste, Italy
[9] Institute for Theoretical Physics, Heidelberg University, Philosophenweg 12, D-69120, Heidelberg, Germany
[10] Centre for Astrophysics and Supercomputing, Swinburne University of Technology, Hawthorn, Victoria 3122, Australia
[11] ARC Centre of Excellence for All Sky Astrophysics in 3 Dimensions (ASTRO 3D), Australia
[12] INAF-Osservatorio Astronomico di Trieste, Via G.B. Tiepolo, 11, I-34143 Trieste, Italy
[13] Scuola Normale Superiore, P.zza dei Cavalieri, I-56126 Pisa, Italy
[14] IFPU-Institute for Fundamental Physics of the Universe, via Beirut 2, I-34151 Trieste, Italy
[15] Gemini Observatory, NSF's NOIRLab, 670 N A'ohoku Place, Hilo, HI 96720, USA
[16] Institute of Astronomy and Kavli Institute of Cosmology, University of Cambridge, Madingley Road, Cambridge CB3 0HA, UK
[17] Instituto de Estudios Astrofísicos, Facultad de Ingeniería y Ciencias, Universidad Diego Portales, Avenida Ejercito Libertador 441, Santiago, Chile
[18] Hamburger Sternwarte, Universität Hamburg, Gojenbergsweg 112, D-21029 Hamburg, Germany
Received 2023 November 22; revised 2024 August 23; accepted 2024 September 9; published 2024 November 5

Abstract

The Fe II/Mg II emission line flux ratio in quasar spectra serves as a proxy for the relative Fe to α-element abundances in the broad-line regions of quasars. Due to the expected different enrichment timescales of the two elements, they can be used as a cosmic clock in the early Universe. We present a study of the Fe II/Mg II ratios in a sample of luminous quasars exploiting high-quality near-IR spectra taken primarily by the XQR-30 program with VLT XSHOOTER. These quasars have a median bolometric luminosity of $\log(L_{\rm bol}[{\rm erg\ s^{-1}}]) \sim 47.3$ and cover a redshift range of $z = 6.0$–6.6. The median value of the measured Fe II/Mg II ratios is ∼7.9 with a normalized median absolute deviation of ∼2.2. In order to trace the cosmic evolution of Fe II/Mg II in an unbiased manner, we select two comparison samples of quasars with similar luminosities and high-quality spectra from the literature, one at intermediate redshifts ($z = 3.5$–4.8) and the other at low redshifts ($z = 1.0$–2.0). We perform the same spectral analysis for all these quasars, including the usage of the same iron template, the same spectral fitting method, and the same wavelength fitting windows. We find no significant redshift evolution in the Fe II/Mg II ratio over the wide redshift range from $z = 1$ to 6.6. The result is consistent with previous studies and supports the scenario of a rapid iron enrichment in the vicinity of accreting supermassive black holes at high redshift.

Unified Astronomy Thesaurus concepts: Quasars (1319); High-redshift galaxies (734); High-luminosity active galactic nuclei (2034)

Materials only available in the online version of record: figure set, machine-readable tables

1. Introduction

The first-generation galaxies and quasars formed and lit up the dark Universe with ionizing photons when the age of the Universe was less than 1 Gyr. High-redshift ($z \gtrsim 6$) quasars provide a direct probe of this epoch of cosmic reionization thanks to their high luminosities (e.g., G. D. Becker et al. 2015; S. E. I. Bosman et al. 2022). In the past two decades, a number of quasars at $z \sim 6$–7.5 have been discovered (e.g., X. Fan et al. 2001; L. Jiang et al. 2007; C. J. Willott et al. 2010; B. P. Venemans et al. 2013; S. L. Reed et al. 2015; E. Bañados et al. 2016; L. Jiang et al. 2016; E. Bañados et al. 2018; Y. Matsuoka et al. 2018; F. Wang et al. 2019, 2021; Y. Matsuoka et al. 2022). Most of those high-redshift luminous quasars host supermassive black holes (SMBHs) with BH masses $M_{\rm BH} \sim 10^{9-10} M_{\odot}$, accreting near the Eddington limit (e.g., E. P. Farina et al. 2022; C. Mazzucchelli et al. 2023). The dense gas orbiting around SMBHs in the broad-line region (BLR) is observed as broad emission lines with the typical full width at half maximum (FWHM) ≈2000–10,000 km s^{-1} at rest-frame UV and optical wavelengths. Photoionization models suggest that the flux ratios of broad emission lines such as N V/C IV, N V/He II and (Si IV+O IV)/C IV can be used to estimate the BLR metallicity (F. Hamann et al. 2002; T. Nagao et al. 2006, but also see M. J. Temple et al. 2021 for the influence of nonabundance parameters). While the BLR metallicity is

[19] Kavli Astrophysics Fellow.

expected to reflect the star formation history of the quasar host galaxy, current observations suggest no significant redshift evolution of the metallicity at redshift up to $z \sim 7.5$ (e.g., T. Nagao et al. 2006; L. Jiang et al. 2007; Y. Juarez et al. 2009; G. D. Rosa et al. 2011, 2014; C. Mazzucchelli et al. 2017; J.-J. Tang et al. 2019; M. Onoue et al. 2020; J.-T. Schindler et al. 2020; S. Lai et al. 2022; S. Wang et al. 2022).

Among all BLR line flux ratios, the ratio of the Fe II pseudo continuum in the rest-frame UV to the Mg II doublet at rest-frame 2798 Å (Fe II/Mg II λ2798) is of particular interest. Mg, an α-element, is enriched mainly by core-collapse type II supernovae (SNe II) soon after the onset of star formation (e.g., S. E. Woosley & R. D. Hoffman 1992). Fe is thought to be efficiently produced by type Ia supernovae (SNe Ia) that evolve from binary systems with a longer lifetime $\sim$1 Gyr (e.g., L. Greggio & A. Renzini 1983). The enrichment timescale of Fe is thus delayed by $\sim$1 Gyr relative to that of Mg. This time delay of the Fe enrichment can serve as a cosmic clock (e.g., F. Hamann & G. Ferland 1993, 1999). Given that $z \geqslant 6$ quasars have reached the first billion years of the Universe, one expects to see a rapid decline of their Fe II/Mg II at $z > 6$, which is sensitive to the star formation history in quasar host galaxies. Observationally, no obvious redshift evolution has been reported at redshift up to $z \sim 7.5$ (e.g., K. Kawara et al. 1996; Y. Yoshii et al. 1998; K. L. Thompson et al. 1999; M. Dietrich et al. 2002; F. Iwamuro et al. 2002; A. J. Barth et al. 2003; M. Dietrich et al. 2003; W. Freudling et al. 2003; R. Maiolino et al. 2003; F. Iwamuro et al. 2004; Y. Tsuzuki et al. 2006; L. Jiang et al. 2007; J. D. Kurk et al. 2007; G. D. Rosa et al. 2011, 2014; C. Mazzucchelli et al. 2017; H. Sameshima et al. 2017; J. Shin et al. 2019; M. Onoue et al. 2020; H. Sameshima et al. 2020; J.-T. Schindler et al. 2020; J. Shin et al. 2021; J. Yang et al. 2021; S. Wang et al. 2022; Y. Yoshii et al. 2022). Based on the nonevolution of Fe II/Mg II, it has been suggested that there are other mechanisms for the Fe production, such as the presence of Population-III stars (M. Onoue et al. 2020; D. Toyouchi et al. 2022; Y. Yoshii et al. 2022).

In previous studies of the Fe II/Mg II redshift evolution, quasar samples and spectral analysis methods are often heterogeneous. Comparison samples at different redshifts were usually from different studies, which may introduce systematic uncertainties or even biases. For example, different studies usually used different spectral fitting methods and different iron emission templates (e.g., C. Mazzucchelli et al. 2017; J. Shin et al. 2019). M. Onoue et al. (2020) showed that different templates of the UV Fe II pseudo continuum introduce an offset of 37% in Fe II/Mg II (see also e.g., J.-H. Woo et al. 2018; J.-T. Schindler et al. 2020). In addition, different studies often used different wavelength ranges or spectral windows for emission-line fitting (e.g., L. Jiang et al. 2007; H. Sameshima et al. 2017; S. Wang et al. 2022). This was limited by the spectra available for different redshifts. The impact of all above factors on the Fe II/Mg II measurement is not well understood. Therefore, it is critical to measure the Fe II/Mg II of quasars at a wide redshift range based on a unified approach.

This paper presents our Fe II/Mg II measurements of $6.0 \lesssim z \lesssim 6.6$ quasars using high-quality spectra taken by a large spectroscopic campaign of VLT/XSHOOTER. The high-redshift sample is compared with intermediate-redshift ($z \sim 4$) and low-redshift ($z \sim 1.5$) samples in order to address the Fe II/Mg II evolution over cosmic time. The structure of the paper is as follows. We introduce our data sets and method of spectral analyses in Sections 2 and 3 respectively. The results of our Fe II/Mg II measurements are shown in Section 4. We discuss the systematic uncertainties and implications of our results in Section 5 and summarize the paper in Section 6. In this paper, we adopt a standard ΛCDM cosmology with $H_0 = 70\,\mathrm{km\,s^{-1}\,Mpc^{-1}}$, $\Omega_\mathrm{m} = 0.3$, and $\Omega_\Lambda = 0.7$. All the magnitudes are reported in the AB system.

2. Data and Quasar Sample

2.1. The Enlarged XQR-30 Quasar Sample

XQR-30 is an European Southern Observatory (ESO) large program (ID:1103.A-0817, P.I. V. D'Odorico; V. D'Odorico et al. 2023) that spent $\sim$250 hr of observing time with the XSHOOTER spectrograph (J. Vernet et al. 2011) at the Very Large Telescope (VLT). The program provides high-quality spectra of 30 quasars at $5.8 \leqslant z \leqslant 6.6$ in the optical and near-infrared wavelengths. These quasars are the brightest $z \geqslant 5.8$ quasars accessible from the Paranal Observatory known by 2018. The mean J-band magnitude of this sample is 19.44 mag. The observations were carried out with a 0.″9-wide slit in the VIS (visible) arm and a 0.″6-wide slit in the NIR (near-infrared) arm. This configuration yields the nominal spectral resolution of $R \sim 8900$ in the optical and $R \sim 8100$ in the near-infrared. An additional set of 12 quasar spectra in the same redshift and luminosity ranges were retrieved from the XSHOOTER archive. These spectra have comparable data quality (e.g., G. D. Becker et al. 2015; S. E. I. Bosman et al. 2018; J.-T. Schindler et al. 2020). The combination of this sample and the main XQR-30 sample, named as the *enlarged* XQR-30 sample (hereafter, E-XQR-30), consists of 42 spectra with a total exposure times of $\sim$350 hr. The median effective resolving power of E-XQR-30 is $R \sim 11{,}400$ and 9800 in the VIS and NIR arms, respectively. The data reduction of the E-XQR-30 sample was performed using a modified version of a custom IDL pipeline (G. D. Becker et al. 2012; S. López et al. 2016; G. D. Becker et al. 2019). This pipeline provides optimal spectral extraction, telluric correction, and sky subtraction (particularly in the near-infrared range), which is optimal for our science goal (S. Noll et al. 2012; A. Jones et al. 2013). The E-XQR-30 NIR spectra are not corrected for Galactic extinction, whose effect is typically negligible at the observed wavelength (V. D'Odorico et al. 2023). More details of the E-XQR-30 quasars and data reduction can be found in V. D'Odorico et al. (2023).

We used the NIR-arm spectra (0.98–2.48 μm) of the E-XQR-30 quasars for our analyses, since the Fe II and Mg II emission lines are redshifted to the near-infrared wavelengths at $z > 6$. These quasars have mean signal-to-noise ratios (SNRs) per pixel above 20 at 2750–2850 Å. We removed DELS J1535+1943 from our final sample because its dust-reddened continuum (J. Yang et al. 2021) cannot be modeled with a single power-law function. We also removed SDSS J0100+2802, one of the external E-XQR-30 quasars discovered by X.-B. Wu et al. (2015), because its line shape of Mg II is strongly affected by the atmospheric absorption at 2.05 μm. There is one gravitationally lensed quasar in our sample, UHS J0439+1634 (X. Fan et al. 2019a), and we take into account the magnification factor of 51.3 reported in X. Fan et al. (2019a). Based on our visual inspection, we further rejected quasars with strong broad absorption lines and quasars

Table 1
The Measured Properties of the E-XQR-30 Quasars

ID	$z_{\rm Mg\ II}$	$J_{\rm AB}$	References	EW Mg II (Å)	FWHM Mg II (km s^{-1})	EW Fe II (Å)	Fe II/Mg II	$\log(\lambda L_{3000})$ (erg s^{-1})	$\log(L_{\rm bol})$ (erg s^{-1})	$L_{\rm bol}/L_{\rm Edd}$	(Fe II/Mg II)$_c$
(1)	(2)	(3)	(4)	(5)	(6)	(7)	(8)	(9)	(10)	(11)	(12)
PSO J158-14	6.065	19.27	(3)	$19.31^{+0.22}_{-0.23}$	2711^{+30}_{-30}	$143.0^{+2.3}_{-2.1}$	$7.41^{+0.13}_{-0.12}$	$46.780^{+0.001}_{-0.002}$	$47.49^{+0.09}_{-0.11}$	$1.83^{+0.45}_{-0.42}$	$4.55^{+0.33}_{-0.26}$
SDSS J0842+1218	6.067	19.70	(3)	$32.46^{+0.30}_{-0.28}$	3238^{+28}_{-27}	$290.4^{+3.0}_{-3.4}$	$8.95^{+0.11}_{-0.10}$	$46.511^{+0.002}_{-0.002}$	$47.22^{+0.09}_{-0.12}$	$0.94^{+0.22}_{-0.22}$	$6.45^{+0.42}_{-0.35}$
PSO J239-07	6.114	19.35	(1)	$29.37^{+0.28}_{-0.25}$	3386^{+30}_{-33}	$244.6^{+2.8}_{-2.4}$	$8.33^{+0.09}_{-0.09}$	$46.684^{+0.001}_{-0.002}$	$47.40^{+0.10}_{-0.12}$	$1.05^{+0.27}_{-0.24}$	$5.84^{+0.42}_{-0.31}$
PSO J217-16	6.135	19.69	(1)	$19.36^{+0.30}_{-0.26}$	3212^{+42}_{-46}	$182.4^{+3.1}_{-2.9}$	$9.42^{+0.18}_{-0.17}$	$46.503^{+0.002}_{-0.002}$	$47.21^{+0.10}_{-0.12}$	$0.95^{+0.25}_{-0.23}$	$6.78^{+0.50}_{-0.39}$
PSO J359-06	6.169	19.85	(1)	$21.43^{+0.36}_{-0.31}$	2446^{+38}_{-35}	$287.0^{+3.2}_{-3.5}$	$13.39^{+0.24}_{-0.23}$	$46.508^{+0.002}_{-0.002}$	$47.22^{+0.10}_{-0.11}$	$1.64^{+0.42}_{-0.36}$	$8.44^{+0.54}_{-0.49}$
PSO J060+24	6.170	19.95	(3)	$17.86^{+0.31}_{-0.34}$	2683^{+53}_{-54}	$141.6^{+2.9}_{-3.1}$	$7.93^{+0.19}_{-0.20}$	$46.489^{+0.002}_{-0.002}$	$47.20^{+0.09}_{-0.11}$	$1.33^{+0.33}_{-0.30}$	$5.25^{+0.37}_{-0.32}$
VDES J2211-3206	6.330	19.54	(3)	$28.86^{+0.41}_{-0.41}$	3123^{+41}_{-40}	$229.1^{+5.3}_{-5.3}$	$7.94^{+0.14}_{-0.17}$	$46.703^{+0.003}_{-0.003}$	$47.41^{+0.10}_{-0.11}$	$1.26^{+0.31}_{-0.28}$	$5.33^{+0.34}_{-0.32}$
PSO J183+05	6.428	19.77	(2)	$31.70^{+0.69}_{-0.67}$	3502^{+76}_{-79}	$326.1^{+7.1}_{-7.4}$	$10.29^{+0.30}_{-0.28}$	$46.370^{+0.003}_{-0.003}$	$47.08^{+0.10}_{-0.13}$	$0.68^{+0.19}_{-0.16}$	$8.00^{+0.61}_{-0.48}$
VDES J0224-4711	6.525	19.73	(3)	$31.66^{+0.36}_{-0.33}$	3239^{+29}_{-30}	$152.2^{+3.2}_{-3.2}$	$4.81^{+0.09}_{-0.09}$	$46.797^{+0.002}_{-0.002}$	$47.51^{+0.10}_{-0.10}$	$1.30^{+0.34}_{-0.28}$	$3.20^{+0.21}_{-0.19}$
PSO J231-20	6.564	19.60	(3)	$23.06^{+0.46}_{-0.50}$	4179^{+81}_{-68}	$278.6^{+8.5}_{-6.7}$	$12.08^{+0.37}_{-0.27}$	$46.553^{+0.003}_{-0.004}$	$47.26^{+0.09}_{-0.13}$	$0.59^{+0.13}_{-0.16}$	$9.73^{+0.76}_{-0.49}$
PSO J323+12	6.585	19.63	(3)	$37.81^{+0.68}_{-0.60}$	2764^{+41}_{-41}	$303.5^{+8.0}_{-7.0}$	$8.03^{+0.18}_{-0.15}$	$46.543^{+0.003}_{-0.004}$	$47.26^{+0.09}_{-0.12}$	$1.34^{+0.30}_{-0.33}$	$5.31^{+0.37}_{-0.28}$
ULAS J1319+0950	6.117	19.58	(3)	$21.34^{+0.37}_{-0.32}$	3989^{+68}_{-67}	$114.2^{+2.6}_{-3.0}$	$5.35^{+0.15}_{-0.14}$	$46.568^{+0.002}_{-0.002}$	$47.28^{+0.09}_{-0.14}$	$0.66^{+0.15}_{-0.18}$	$4.20^{+0.32}_{-0.21}$
CFHQS J1509-1749	6.119	19.75	(3)	$16.88^{+0.24}_{-0.23}$	3448^{+50}_{-53}	$42.1^{+2.0}_{-2.1}$	$2.49^{+0.13}_{-0.11}$	$46.628^{+0.002}_{-0.002}$	$47.34^{+0.09}_{-0.13}$	$0.95^{+0.22}_{-0.26}$	$1.79^{+0.17}_{-0.11}$
SDSS J1030+0524	6.304	19.87	(3)	$26.99^{+0.36}_{-0.29}$	3161^{+38}_{-36}	$141.3^{+3.4}_{-3.0}$	$5.24^{+0.12}_{-0.11}$	$46.581^{+0.002}_{-0.002}$	$47.29^{+0.09}_{-0.12}$	$1.07^{+0.26}_{-0.25}$	$3.66^{+0.26}_{-0.21}$
VST-ATLAS J025-33	6.330	19.10	(3)	$18.90^{+0.22}_{-0.23}$	3471^{+40}_{-42}	$74.0^{+2.2}_{-2.1}$	$3.91^{+0.10}_{-0.10}$	$46.838^{+0.002}_{-0.001}$	$47.55^{+0.09}_{-0.11}$	$1.19^{+0.26}_{-0.28}$	$2.66^{+0.22}_{-0.14}$
WISEA J0439+1634	6.520	17.47	(3)	$17.60^{+0.06}_{-0.05}$	2982^{+11}_{-11}	$122.3^{+0.3}_{-0.4}$	$6.95^{+0.03}_{-0.03}$	$45.884^{+0.000}_{-0.000}$	$46.60^{+0.09}_{-0.12}$	$0.54^{+0.13}_{-0.13}$	$5.73^{+0.36}_{-0.30}$
PSO J036+03	6.527	19.40	(3)	$5.43^{+0.26}_{-0.26}$	2556^{+112}_{-104}	$44.0^{+3.7}_{-3.5}$	$8.11^{+0.65}_{-0.61}$	$46.808^{+0.003}_{-0.003}$	$47.52^{+0.10}_{-0.11}$	$2.12^{+0.62}_{-0.50}$	$4.81^{+0.58}_{-0.42}$

Note. The Mg II redshifts of the quasars are given in column (2). The *J*-band magnitudes and their references are listed in columns (3) and (4). The measured FWHM Mg II in unit of km s^{-1} and EW Mg II in unit of Å are listed in columns (5) and (6). The measured EW Fe II in unit of Å is given in column (7). Since the EWs in this study were derived from scaled flux, the Fe II/Mg II (column (9)) are equal to the flux ratios. The rest-frame continuum luminosity λL_{3000}, the bolometric luminosity $L_{\rm bol}$ and the Eddington ratio $L_{\rm bol}/L_{\rm Edd}$ are listed in columns (9)–(11). The Fe II/Mg II results after correcting the Eddington ratio dependence are listed in column (12). The measurement uncertainties were derived from a Monte Carlo simulation based on the flux error at each wavelength step.
References. (1) E. Bañados et al. (2016); (2) C. Mazzucchelli et al. (2017); (3) N. P. Ross & N. J. G. Cross (2020).

(This table is available in machine-readable form in the online article.)

at redshifts $z < 6.05$, whose Mg II emission lines in the spectra are severely affected by the heavy atmospheric absorption at $\sim$1.9 μm. We also rejected PSO J065-26 and PSO J217-07, because their Mg II lines are strongly affected by the atmospheric absorption at $\sim$2 μm. In the end, our E-XQR-30 sample consists of 17 quasars at redshifts between 6.05 and 6.6.

For each selected quasar, its VIS- and NIR-arm spectra were merged with each other using their overlapping spectral region at 1.00–1.02 μm. The merged spectrum was then scaled to match the *J*-band photometry of the quasar. The *J*-band magnitudes of our quasars were collected from the literature (see Table 1; E. Bañados et al. 2016; C. Mazzucchelli et al. 2017; N. P. Ross & N. J. G. Cross 2020). Finally, we rebinned the spectrum by an integer number of pixels using a public code SpectRes (A. C. Carnall 2017) so that all quasar spectra have a fixed wavelength step of 50 km s^{-1}. This step harmonized the resolution of different spectra to reduce systematic bias. The bolometric luminosity was derived by applying a bolometric correction of $L_{\rm bol} = 5.15 \times \lambda L_{3000}$ (Y. Shen et al. 2008), where L_{3000} is the luminosity at rest-frame 3000 Å. The typical error in the bolometric correction is $\sim$0.1 dex (G. T. Richards et al. 2006), and this error is propagated into the uncertainty estimate for $L_{\rm bol}$. The median bolometric luminosity of the final sample of E-XQR-30 is $\log(L_{\rm bol}[{\rm erg\ s^{-1}}]) \sim 47.3 \pm 0.1$, where the uncertainty is the normalized median absolute deviation (NMAD). The measured $L_{\rm bol}$ scatter of the E-XQR-30 sample is similar to the propagated uncertainty of each $L_{\rm bol}$. The minimum and median values of the mean SNRs per pixel at the rest-frame 2250–2350 Å of the rebinned spectra are 40 and 52, respectively. Figure 1 shows two examples of the final spectra at rest-frame 2100–3100 Å.

2.2. The XQ-100 Quasar Sample

The intermediate-redshift sample is from XQ-100, another VLT/XSHOOTER large program of ESO (ID:189.A-0424, P.I. S. López; S. López et al. 2016). XQ-100 provides 100 high-quality quasar spectra at $z \sim 3.5$–4.8. The adopted slit widths were 1.″0 in the UVB arm and 0.″9 in the VIS and NIR arms, providing the nominal resolution of 5400, 8900, and 5600, respectively. The data reduction of XQ-100 was done using a custom IDL pipeline similar to that for E-XQR-30. The XQ-100 spectra are also not corrected for Galactic extinction for the same reason as E-XQR-30. The reduced data were retrieved from the ESO archive. From the XQ-100 sample, we selected 78 quasars at $3.5 < z < 4.8$ whose Mg II emission lines are not severely affected by the atmospheric absorption at 1.35–1.42 μm. We thus removed quasars at $z = 3.82$–4.08. We also removed another quasar (J0747+2739) whose telluric absorption is not well corrected.

The XQ-100 spectra were merged, scaled, and rebinned using the same methods as for the E-XQR-30 spectra. We referred to the *J*-band photometry reported in existing NIR surveys, including the VISTA Hemisphere Survey (R. G. McMahon et al. 2013), VISTA Kilo-degree Infrared Galaxy Survey (A. Edge et al. 2013), UKIRT Hemisphere Survey (S. Dye et al. 2018), UKIDSS Large Area Survey (A. Lawrence et al. 2007), and Two Micron All Sky Survey

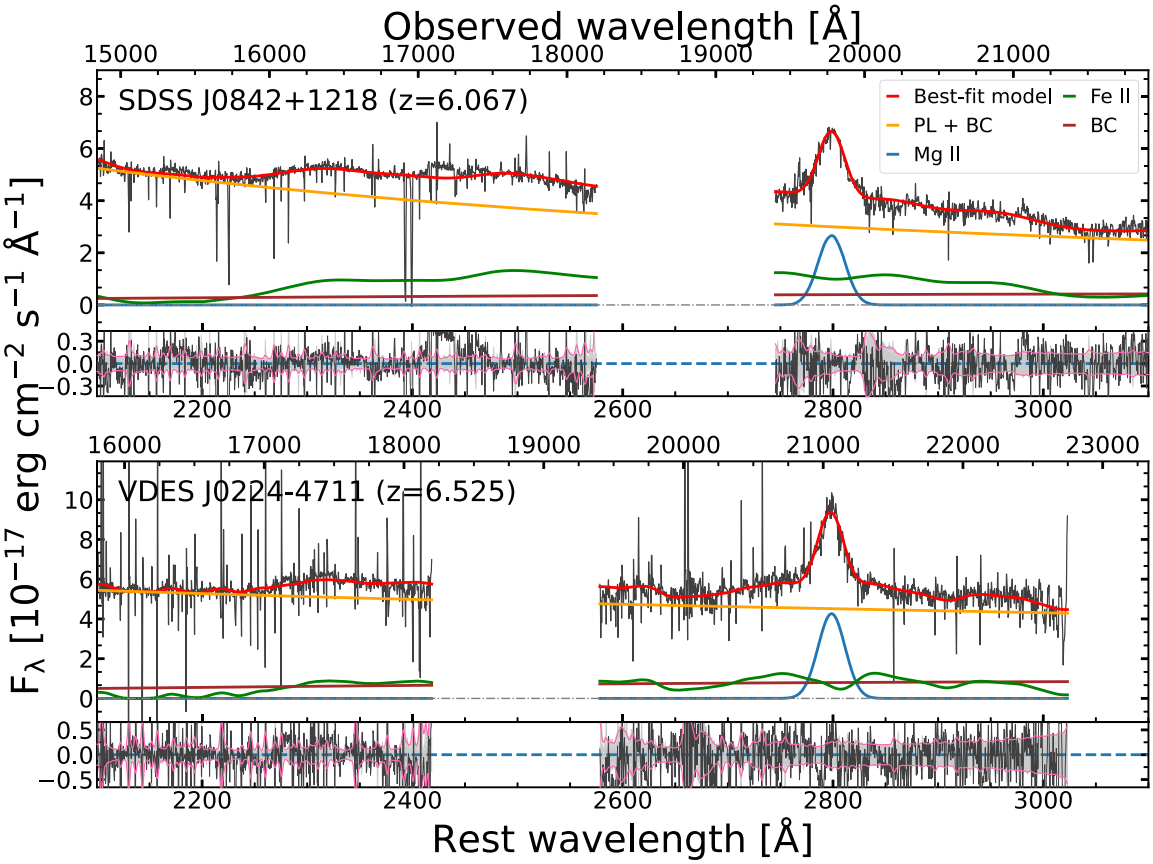

Figure 1. Spectral fitting for two representative spectra in the E-XQR-30 sample at $\lambda_{\rm rest} \sim 2100$–$3100$ Å. The heavy atmospheric absorption regions at 18200–19400 Å are masked out in the figure. In each panel, the color-coded lines show the power-law continuum plus Balmer continuum (PL + BC, orange), the Balmer continuum only (BC, brown), the scaled Fe II template from Y. Tsuzuki et al. (2006) (Fe II, green), and the Mg II emission line (Mg II, blue). The red line shows the sum of all components (best-fit model). For each spectrum, the residual flux of the best-fit model with the $\pm 1\sigma$ observed errors (gray ranges) is shown in the lower subpanel. We also smooth the errors and use the pink curves to indicate their boundaries. The full list of the spectra with the best-fit model fits are published as online figures, and the captions of the online figures are the same as the caption of this figure (but for different quasars).

(The complete figure set (17 images) is available in the online article.)

Point Source Catalog (R. M. Cutri et al. 2003). The exact reference of each quasar is reported in Table 2. The median bolometric luminosities of the XQ-100 sample is $\log(L_{\rm bol}[{\rm erg\ s^{-1}}]) \sim 47.5 \pm 0.2$, which is similar to that of E-XQR-30. The minimum and median values of the mean SNRs per pixel at rest-frame 2250–2350 Å of this sample are 30 and 70, respectively, which are comparable to the SNRs of the E-XQR-30 spectra. Figure 2 shows two examples of the spectra.

2.3. The SDSS DR16 Quasar Sample

We selected our low-redshift sample from the Data Release 16 of the Sloan Digital Sky Survey quasar catalog (hereafter, SDSS DR16Q; B. W. Lyke et al. 2020). The SDSS DR16Q spectra are all corrected for Galactic extinction using the dust map of D. J. Schlegel et al. (1998) by B. W. Lyke et al. (2020). The spectral resolution of the SDSS DR16Q quasar spectra is $R \sim 2000$ (150 km s^{-1} per each resolution element), which is lower than the resolutions of E-XQR-30 and XQ-100. We tested the effect of the resolution using $z > 6.05$ E-XQR-30 quasar spectra, whose Mg II emission lines are free from the atmospheric absorption window and thus more closely resemble the SDSS spectral situation. We degraded the E-XQR-30 quasar spectra with a Gaussian kernel to reduce the spectral resolutions from their effective resolutions reported in V. D'Odorico et al. (2023) to 2000. The median Fe II/Mg II value of the degraded sample is only 2% lower than that of the original sample, within 0.15 σ significance.

The comparison of the Fe II/Mg II values is presented in Appendix A. Therefore, we concluded that the relatively low spectral resolution of the SDSS DR16Q sample does not affect our measurements of Fe II/Mg II.

We chose SDSS DR16Q quasars that have similar bolometric luminosities as the E-XQR-30 and XQ-100 quasars. We first used the median SNRs of the SDSS spectra provided by the DR16Q catalog to select high-quality spectra, requiring median SNRs higher than 20 per pixel. We also limited our low-redshift range to $0.81 < z < 1.97$ so that the SDSS spectra cover the rest-frame 2100–3100 Å. This redshift range is slightly different from that of H. Sameshima et al. (2017), who used the SDSS spectra at $0.72 < z < 1.63$ to perform Fe II/Mg II measurements. This is because the spectral window for their emission-line fitting, the rest-frame 2200–3500 Å, is different from ours. We will discuss the effect of these two different spectral windows in Section 5.1. For each quasar in the sample, we scaled its spectrum to match the r-band photometry of the quasar. We then fitted the spectrum to measure L_{3000} and computed the bolometric luminosity from

Table 2
The Measured Properties of the XQ-100 Quasars

ID	$z_{\rm Mg\ II}$	$J_{\rm AB}$ (mag)	Reference	Flag	EW Mg II (Å)	FWHM Mg II (km s^{-1})	EW Fe II (Å)	Fe II/Mg II	$\log(\lambda L_{3000})$ (erg s^{-1})	$\log(L_{\rm bol})$ (erg s^{-1})	$L_{\rm bol}/L_{\rm Edd}$	$({\rm Fe\ II/Mg\ II})_c$
(1)	(2)	(3)	(4)	(5)	(6)	(7)	(8)	(9)	(10)	(11)	(12)	(13)
J133254+005250	3.509	17.84	(2)	1	$18.61^{+0.09}_{-0.08}$	2511^{+13}_{-15}	$89.6^{+1.0}_{-1.5}$	$4.81^{+0.06}_{-0.07}$	$46.804^{+0.001}_{-0.001}$	$47.52^{+0.09}_{-0.13}$	$2.19^{+0.50}_{-0.54}$	$2.83^{+0.20}_{-0.16}$
HB89 1159+123	3.516	16.71	(2)	0	$30.48^{+0.09}_{-0.09}$	3119^{+10}_{-10}	$254.9^{+1.3}_{-1.3}$	$8.36^{+0.04}_{-0.04}$	$47.184^{+0.001}_{-0.001}$	$47.90^{+0.10}_{-0.11}$	$2.20^{+0.56}_{-0.50}$	$4.91^{+0.35}_{-0.27}$
SDSS J1024+1819	3.520	17.88	(5)	0	$21.35^{+0.23}_{-0.27}$	4048^{+43}_{-53}	$95.1^{+3.0}_{-3.2}$	$4.45^{+0.15}_{-0.13}$	$46.782^{+0.001}_{-0.002}$	$47.49^{+0.09}_{-0.12}$	$0.82^{+0.20}_{-0.20}$	$3.32^{+0.28}_{-0.19}$
J101818+054822	3.521	18.50	(2)	1	$27.04^{+0.16}_{-0.15}$	3575^{+23}_{-21}	$109.0^{+2.0}_{-2.0}$	$4.03^{+0.07}_{-0.07}$	$46.540^{+0.001}_{-0.001}$	$47.25^{+0.09}_{-0.13}$	$0.80^{+0.17}_{-0.21}$	$3.02^{+0.22}_{-0.16}$
J144250+092001	3.536	17.38	(2)	1	$19.44^{+0.10}_{-0.11}$	5118^{+34}_{-33}	$60.1^{+1.1}_{-1.3}$	$3.09^{+0.06}_{-0.06}$	$47.015^{+0.001}_{-0.001}$	$47.73^{+0.10}_{-0.11}$	$0.67^{+0.17}_{-0.15}$	$2.41^{+0.16}_{-0.13}$

Note. The same table as Table 1 but for the XQ-100 sample. The column (5) lists the flags of whether there is a suspicious arm-connection problem in this spectrum at <2200 Å, with 0 indicating normal and 1 indicating a problem. Only a fraction of the XQ-100 sample are presented here.

References. (1) R. M. Cutri et al. (2003), (2) A. Lawrence et al. (2007), (3) A. Edge et al. (2013), (4) R. G. McMahon et al. (2013), (5) S. Dye et al. (2018).

(This table is available in its entirety in machine-readable form in the online article.)

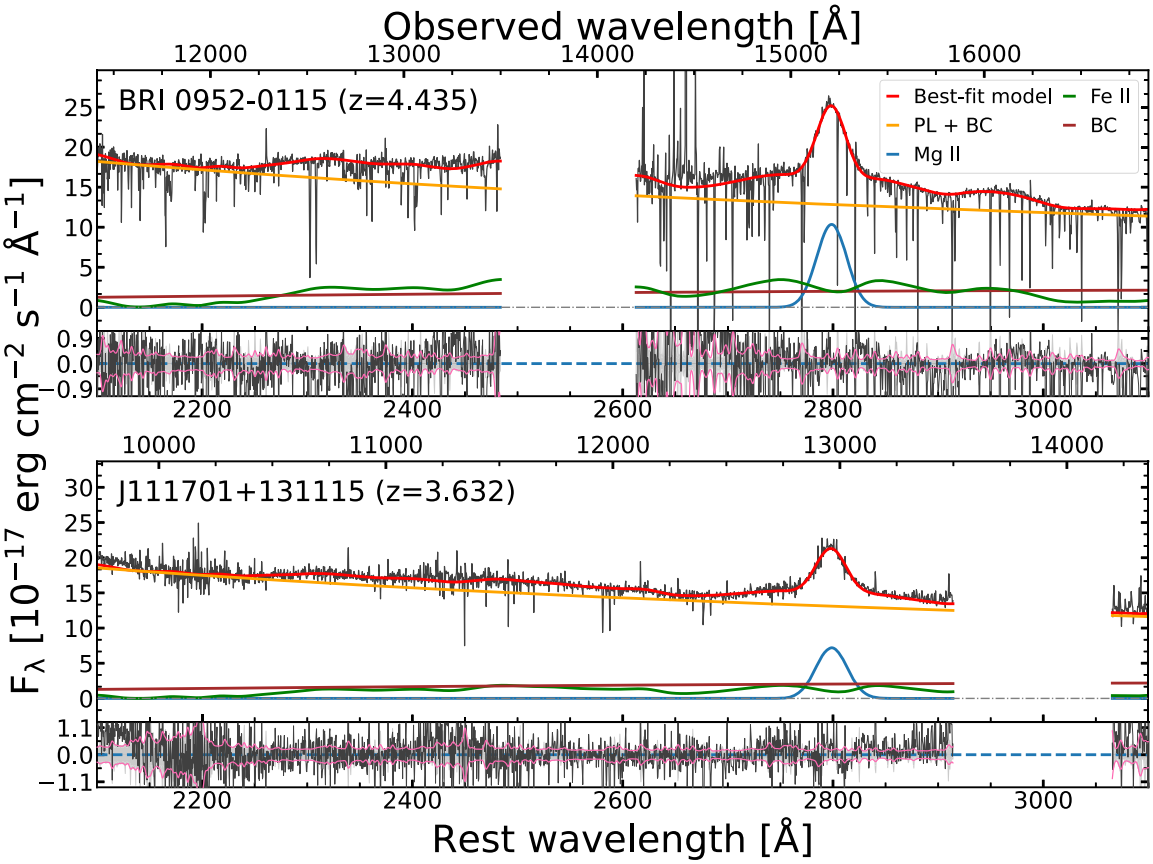

Figure 2. Same as Figure 1 but for the XQ-100 sample. The heavy atmospheric absorption regions at 13500–14200 Å are masked out in the figure. The Fe II/Mg II ratios of BRI 0952-0115 (upper panel) and J111701 + 131115 (lower panel) are $5.15^{+0.04}_{-0.04}$ and $3.74^{+0.09}_{-0.08}$, respectively. The full list of the spectra with the best model fits are published as online figures. For the XQ-100 spectra that show flux correction problems as described in Section 3, they are labeled with Flag = 1 in Table 2 and their affected wavelength regions are marked with a red bar in the online figures.

(The complete figure set (78 images) is available in the online article.)

L_{3000}. We selected 1291 SDSS quasars in the bolometric luminosity range of log ($L_{\rm bol}$[erg s^{-1}]) ∼ 47.0–48.0.

We selected our final low-redshift sample from these 1291 high-luminosity SDSS quasars, forcing it to follow the luminosity distribution of the E-XQR-30 and XQ-100 samples. This procedure enables us to have a better control over the three quasar samples at different redshift ranges. To achieve this goal, we extracted a luminosity-matched sample of 99 quasars from the SDSS quasars. The selected sample size is limited by the small number of high-luminosity quasars (log ($L_{\rm bol}$[erg s^{-1}]) > 47.5) in the 1291 SDSS quasars. These 99 SDSS quasars span a redshift range of $0.95 \leqslant z \leqslant 1.97$, and their minimum and median values of the mean SNRs per pixel at rest-frame 2250–2350 Å are 24 and 39, respectively. Figure 3 shows two examples of the spectra. Figure 4 shows the bolometric luminosity distribution of the three samples as a function of redshift.

3. Spectral Analyses

We carried out multicomponent spectral fitting for the three quasar samples introduced in Section 2. For each quasar, its observed continuum was decomposed into a power-law continuum ($F_{\rm PL} = F_0 \lambda^{\alpha_\lambda}$), a Balmer continuum ($F_{\rm BC}$), and an iron pseudo continuum, with three free parameters, namely the scale factor and the slope of a single power-law function, and the scale factor of the UV iron template. To measure the Fe II flux, we used the empirical iron template from Y. Tsuzuki et al. (2006; hereafter the T06 iron template). The T06 iron template is based on a high resolution spectrum of I Zw I, a narrow-line Seyfert 1 galaxy at $z = 0.061$. This template has been frequently used in the literature (e.g., H. Sameshima et al. 2017; J. Shin et al. 2019; M. Onoue et al. 2020; J.-T. Schindler et al. 2020; J. Shin et al. 2021; S. Wang et al. 2022). It is also suited for our analyses, because it takes into account the Fe II contribution underneath Mg II based on photoionization models. The iron template was convolved with Gaussian kernels to generate a range of line widths of FWHM = 500–10,000 km s^{-1}, with a step size of 500 km s^{-1}.

For the underlying Balmer continuum, we adopted the following formula introduced by S. A. Grandi (1982),

$$F_{\rm BC} = F_{\rm BE}\, B_\lambda(T_e)\, (1 - e^{-\tau_e(\lambda/\lambda_{\rm BE})^3}), \quad (1)$$

where $B_\lambda(T_e)$ is the Planck function at an electron temperature T_e and τ_e is the optical depth at the Balmer edge $\lambda_{\rm BE} = 3646$ Å. Owing to the limited wavelength coverage, we followed previous studies (e.g., M. Dietrich et al. 2003; J. D. Kurk et al. 2007; G. D. Rosa et al. 2011; C. Mazzucchelli et al. 2017; J. Shin et al. 2019; M. Onoue et al. 2020; J.-T. Schindler et al. 2020; S. Wang et al. 2022) and fixed the normalization factor $F_{\rm BE}$ to be 30% of $F_{\rm PL}(\lambda = 3675$ Å). The two parameters T_e and τ_e were fixed to be 15,000 K and 1, respectively, following the literature (e.g., G. D. Rosa et al. 2011; C. Mazzucchelli et al. 2017; J. Shin et al. 2019; M. Onoue et al. 2020; J.-T. Schindler et al. 2020). These

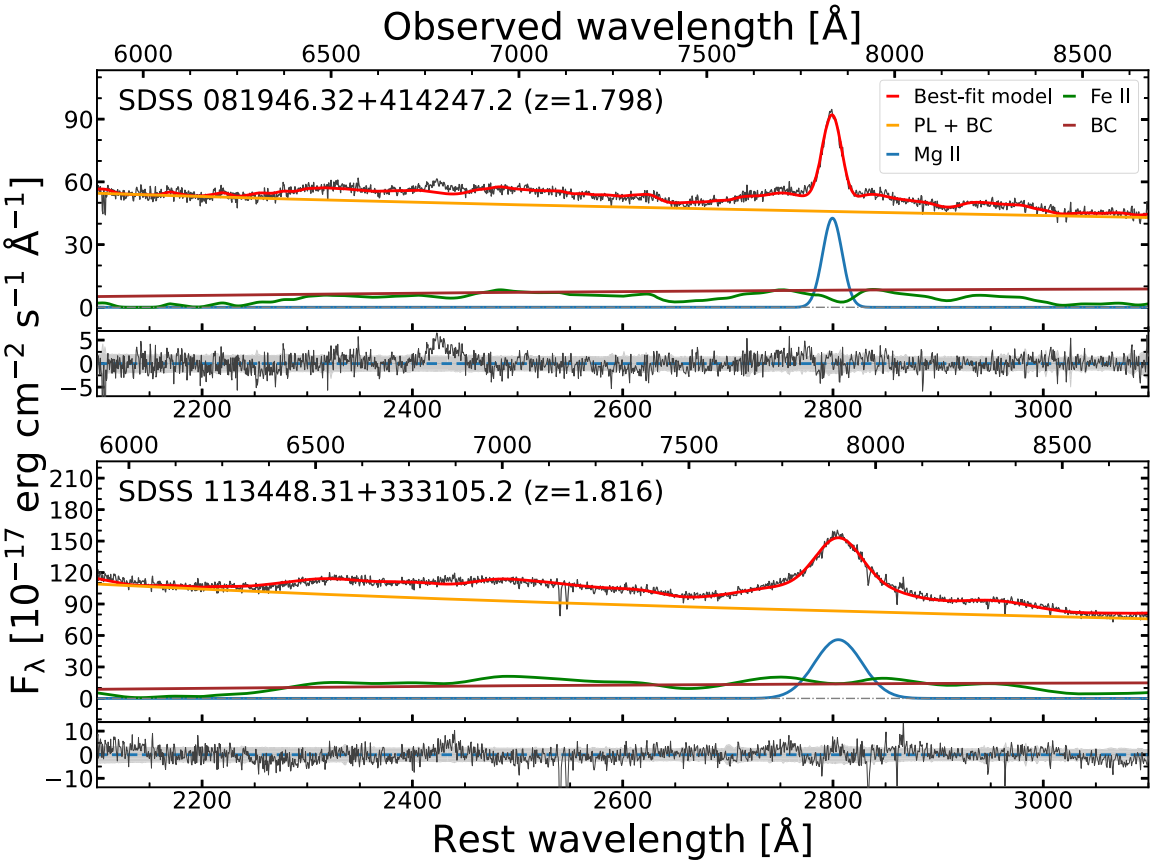

Figure 3. Same as Figure 1 but for the low-redshift SDSS sample. The smoothed errors are not shown for SDSS spectra. The Fe II/Mg II ratios of SDSS 081946.32+414247.2 (upper panel) and SDSS 113448.31+333105.2 (lower panel) are $4.31^{+0.09}_{-0.10}$ and $3.75^{+0.06}_{-0.07}$, respectively.

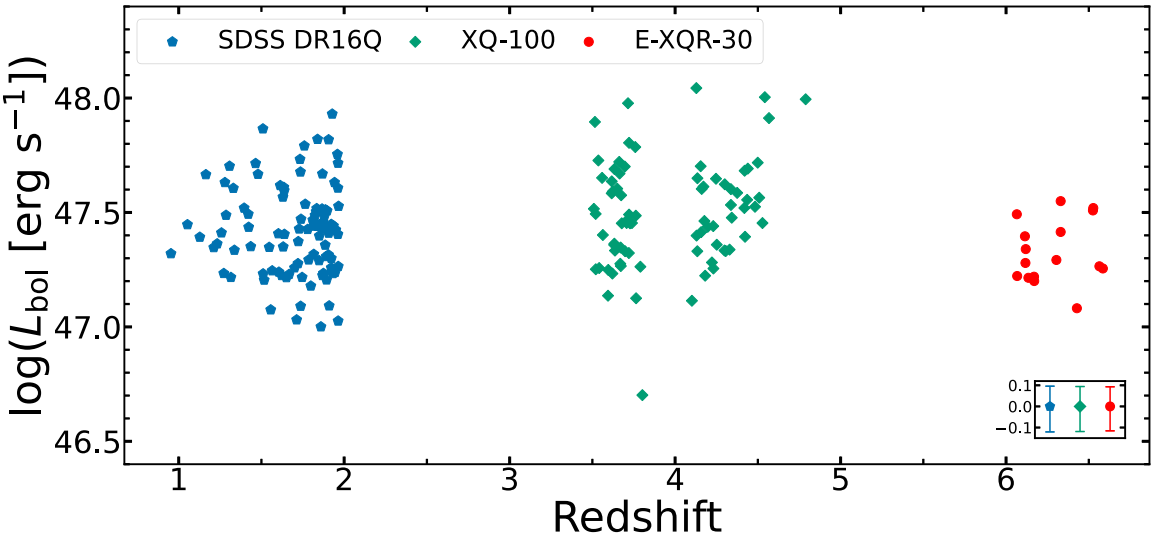

Figure 4. The redshift—bolometric luminosity plane of the three quasar samples used in this work. The red circles, green diamonds, and blue pentagons represent the E-XQR-30 quasars at $6.0 \leqslant z \leqslant 6.6$, the XQ-100 quasars at $3.5 \leqslant z \leqslant 4.8$, and the low-redshift SDSS quasars, respectively. Their typical measurement errors of $\log L_{\rm bol}$ are shown in the lower right corner. These quasars are among the most luminous quasar populations at these epochs ($47.0 \lesssim \log L_{\rm bol}$ [ergs^{-1}] $\lesssim 48.0$).

choices can help us avoid systematic differences when we compare with previous results later.

We generated a model to fit the spectrum with the single power-law continuum, the Balmer continuum, and the T06 iron template. The fitting method is similar to that described in M. Onoue et al. (2020), and is slightly modified to suit our three samples and science goals. The VIS and NIR arms of XSHOOTER cover a wide wavelength range of 550–2480 nm. To focus on Fe II and Mg II in this study and optimize our results, we chose to fit the NIR-arm spectrum only. The employed continuum+iron fitting windows are $\lambda_{\rm rest} = 2100$–$2750$ Å and 2850–3100 Å. The robustness of the continuum measurement in this spectral range is discussed in Section 5.2. We excluded the strong atmospheric absorption ranges for each E-XQR-30 and

XQ-100 spectrum, and modified the longest wavelengths fitted for some spectra due to their limited spectral coverage. A small number of the XQ-100 spectra displayed a glitch in the connection region between the NIR and VIS arms, due to a wavelength-dependent flux correction problem. This will likely affect our measurements of the continuum and Fe II/Mg II values. We visually checked the spectra and adjusted the continuum +iron fitting windows for these spectra. Wavelength regions with suspicious arm-connection problems were excluded. We also flagged them in the XQ-100 online table (see Table 2). All best-fit models performed well near Mg II and in most of the Fe II measurement regions. The results change by only ∼1% without these flagged spectra, suggesting that this has very limited impact on our study. For completeness, we still used the full XQ-100 sample in our analyses. The low-redshift SDSS sample did not change because it has no strong atmospheric absorption bands. These fitting windows cover some weak emission lines such as [C II] λ2326 and [O II] λ2471, but the distribution of the iron pseudo continuum is much wider than these small emission lines, and thus they do not affect our spectra fitting results.

The quasar spectra were iteratively fitted to obtain the power-law scale and slope factors, and the scale factor of the iron template. We redshifted the iron templates to the Mg II-based redshift, without considering a potential velocity shift. The fitting steps on the continuum+iron windows are described below.

1. A single power-law continuum plus Balmer continuum were fitted to the spectrum.
2. The iron template was fitted to the continuum-subtracted spectrum.
3. The continuum model was updated by repeating the continuum fitting to the spectrum after subtracting the iron model.

All fitting steps above used the least-square method. The second and third steps were repeated until the three parameters achieved <1% convergence. In the procedure, we used all iron templates with different line widths, and selected one iron model that returned the minimum χ^2 value at the continuum +iron windows. The broad Mg II emission line was then fitted to the residual spectrum after subtracting the best-fit continuum +iron model. A single Gaussian profile was used to fit the emission line. The two Mg II double emission lines mix together due to the broad-line width, so a single Gaussian profile is sufficient for the fit. The fitting window for Mg II was $\lambda_{\rm rest} = 2750$–$2850$ Å.

We ran the above procedure twice. After the completion of the first iteration, we used the best-fit models to perform a single round of 3σ clipping to mask out the pixels that could be significantly affected by strong sky lines or cosmic rays. The sigma is the observed flux error. We then performed the second iteration after the sigma clipping. Figures 1, 2, and 3 show a few examples of the high-redshift E-XQR-30, intermediate-redshift XQ-100, and low-redshift SDSS spectra with their best-fit models, respectively.

The Fe II flux was calculated by integrating the scaled iron template over $2200 \leqslant \lambda_{\rm rest}$ [Å] $\leqslant 3090$. The equivalent widths (EWs) of the Fe II and Mg II emission lines were derived by dividing the line flux by the power law plus Balmer continuum flux at $\lambda_{\rm rest} = 3000$ Å. This procedure is to make a direct comparison with H. Sameshima et al. (2017) and M. Onoue et al. (2020), who measured EWs in the same way. We also calculated the Fe II and Mg II EWs using the standard EW measurement. The differences of the measured EWs from the two methods are only 0.06–0.08 dex, and are much smaller than the measurement errors. The monochromatic luminosity λL_{3000} and bolometric luminosity $L_{\rm bol}$ were measured using the method described in Section 2.1.

We propagated the measurement uncertainties using Monte Carlo simulations. Specifically, we generated 1000 mock spectra for each quasar. The flux at each wavelength was the original flux plus an error flux. The error flux was randomly drawn from a Gaussian distribution with σ equal to the observed error at this wavelength. We repeated our fitting process for each version of the noise-added spectrum. We obtained a distribution of the 1000 results for each continuum +emission parameter, and their 1σ uncertainties were measured from the 16th and 84th percentiles of the distribution.

4. Results

4.1. Emission-line Properties

The Fe II and Mg II broad emission-line properties are derived from our best-fit models. With our Mg II measurement using the T06 iron template, we estimate the Eddington luminosities of the quasars in all samples by the following formula

$$L_{\rm Edd} = 1.3 \times 10^{38} \left(\frac{M_{\rm BH}}{M_\odot} \right) {\rm erg\ s^{-1}}, \quad (2)$$

where $M_{\rm BH}$ is the BH mass calculated using the virial relation from M. Vestergaard & P. S. Osmer (2009). The Eddington ratio $L_{\rm bol}/L_{\rm Edd}$ is obtained by dividing the bolometric luminosity by the Eddington luminosity. The uniform measurements of the Eddington ratios for our three redshift samples help us correct the correlation between the Fe II/Mg II ratio and the Eddington ratio (see Section 4.2). The measurement uncertainties of these quantities are derived from the same Monte Carlo simulations as described in Section 3. We calculate these ratios from the 1000 mock spectra of each quasar and obtain their distributions. The 1σ uncertainties are measured from the 16th and 84th percentiles of the distributions.

The measured properties of the E-XQR-30 quasars are presented in Table 1. The emission-line properties of the low-redshift and intermediate-redshift samples are measured in the same way. The measured properties of the XQ-100 and SDSS samples are shown in Tables 2 and 3 respectively, with machine-readable formats available online.

4.2. Dependence on the Eddington Ratio

The Fe II/Mg II flux ratio has been used as a proxy for the Fe/Mg abundance ratio (i.e., [Fe/α]). It is expected to show a dramatic change at cosmic age ∼1 Gyr due to the different evolution timescales of SNe Ia and SNe II, the major producers of Fe and Mg respectively (e.g., F. Hamann & G. Ferland 1993, 1999). On the other hand, observations have shown that the Mg II EW anticorrelates with the Eddington ratio (X.-B. Dong et al. 2011; H. Sameshima et al. 2017). This dependence on the nonabundance parameter has to be corrected when one addresses the chemical enrichment of the BLR cloud. Photoionization models show that this Eddington ratio dependence can be attributed to the different origin of the Fe II and Mg II emission. H. Sameshima et al. (2017) argued that Mg II mainly originates from the fully ionized zone

Table 3
The Measured Properties of the SDSS Quasars

ID	$z_{\rm Mg\ II}$	r[a] (mag)	EW Mg II (Å)	FWHM Mg II (km s^{-1})	EW Fe II (Å)	Fe II/Mg II	$\log(\lambda L_{3000})$ (erg s^{-1})	$\log(L_{\rm bol})$ (erg s^{-1})	$L_{\rm bol}/L_{\rm Edd}$	$({\rm Fe\ II/Mg\ II})_c$
(1)	(2)	(3)	(4)	(5)	(6)	(7)	(8)	(9)	(10)	(11)
SDSS135823.98+021343.8	0.953	15.73	$12.49^{+0.14}_{-0.17}$	4374^{+76}_{-77}	$82.1^{+1.4}_{-1.3}$	$6.57^{+0.15}_{-0.13}$	$46.610^{+0.000}_{-0.000}$	$47.32^{+0.11}_{-0.10}$	$0.58^{+0.16}_{-0.12}$	$5.32^{+0.34}_{-0.32}$
SDSS142107.56+253821.0	1.053	15.58	$18.97^{+0.15}_{-0.15}$	2666^{+24}_{-31}	$109.7^{+1.5}_{-1.6}$	$5.78^{+0.09}_{-0.09}$	$46.740^{+0.000}_{-0.000}$	$47.45^{+0.09}_{-0.13}$	$1.79^{+0.44}_{-0.46}$	$3.57^{+0.28}_{-0.21}$
SDSS082045.38+130618.9	1.128	15.92	$13.23^{+0.12}_{-0.11}$	2810^{+25}_{-28}	$86.0^{+1.4}_{-1.5}$	$6.50^{+0.12}_{-0.12}$	$46.680^{+0.000}_{-0.000}$	$47.39^{+0.10}_{-0.13}$	$1.52^{+0.38}_{-0.39}$	$4.18^{+0.31}_{-0.25}$
SDSS120858.01+454035.4	1.164	15.28	$19.15^{+0.16}_{-0.15}$	4256^{+46}_{-42}	$96.7^{+1.5}_{-1.5}$	$5.05^{+0.09}_{-0.09}$	$46.950^{+0.000}_{-0.000}$	$47.67^{+0.09}_{-0.12}$	$0.91^{+0.20}_{-0.22}$	$3.67^{+0.24}_{-0.21}$
SDSS143120.53+395241.5	1.212	16.19	$21.63^{+0.22}_{-0.24}$	5563^{+68}_{-63}	$95.2^{+2.2}_{-1.9}$	$4.40^{+0.11}_{-0.10}$	$46.640^{+0.000}_{-0.000}$	$47.35^{+0.10}_{-0.12}$	$0.37^{+0.09}_{-0.09}$	$3.97^{+0.29}_{-0.23}$

Notes. The same table as Table 1 but for the low-redshift SDSS sample.
[a] The *r*-band magnitudes are quoted from H. Aihara et al. (2011).

(This table is available in its entirety in machine-readable form in the online article.)

(FIZ), while Fe II mainly originates from the partially ionized zone (PIZ). When the gas density increases, the electron temperature of the FIZ decreases, the fraction of Mg^+ increases, and thus the Mg II emitted by the collisional excitation is stronger. Meanwhile, the electron temperature of the PIZ and its Fe^+ and Mg^+ fractions are basically unchanged. In order to correct for this density effect, H. Sameshima et al. (2017) introduced a correction to take into account the Eddington ratio dependence of the observed Fe II/Mg II ratio:

$$\mathrm{EW(Mg\ II)_c} = \mathrm{EW(MgII)}\left(\frac{\langle L_{\rm bol}/L_{\rm Edd}\rangle}{L_{\rm bol}/L_{\rm Edd}}\right)^{a}, \quad (3)$$

where the median value of their measured Eddington ratios is $\langle L_{\rm bol}/L_{\rm Edd}\rangle = 10^{-0.55}$, and the power-law index is $a = -0.30$. We apply this correction to previous samples (except the XQz5 sample; see below) that will be used to compare with our results.

For our samples (i.e., the samples for which we measured the Fe II/Mg II ratio ourselves), we slightly modify the correction, because our spectral fitting windows are different from those of H. Sameshima et al. (2017) and thus there is an offset between the two Fe II/Mg II measurements (see Section 5.1). We perform a linear regression for the 1291 high-luminosity low-redshift SDSS DR16Q quasars to derive a new empirical correlation between the Eddington ratio and the Fe II/Mg II ratio. From our analyses, the median value of the Eddington ratios is $\langle L_{\rm bol}/L_{\rm Edd}\rangle = 10^{-0.62}$ and the power-law index is $a = -0.24 \pm 0.01$. We propagate this uncertainty of the power-law index into the uncertainty estimate for $(\mathrm{Fe\ II/Mg\ II})_c$. We use this new correction in our following analyses, assuming that the Eddington ratio dependence does not evolve with redshift. Figure 5 shows the observed Fe II/Mg II ratios before and after this correction, as well as their linear regressions. We also apply our correction to the XQz5 sample that consists of 83 luminous quasars between $4.5 < z < 5.3$ with optical and near-infrared spectroscopic observations (S. Lai et al. 2024). The luminosity range of this sample is similar to ours. The Fe II/Mg II values of the XQz5 quasars were measured by S. Lai et al. (2023), and were further corrected to match our measurement for a fair comparison.

4.3. No Redshift Evolution of Fe II/Mg II

The Fe II/Mg II flux ratios of our three samples are presented in the top panel of Figure 6. Other measurements that used the T06 iron template and reported Fe II flux at the same wavelength range (2200 Å$\leqslant \lambda_{\rm rest} \leqslant$ 3090 Å) are also shown in the same figure (H. Sameshima et al. 2017; J. Shin et al. 2019; M. Onoue et al. 2020; J.-T. Schindler et al. 2020; J. Shin et al. 2021; S. Wang et al. 2022). The middle panel of Figure 6 shows the Fe II/Mg II line ratios after correcting the Eddington ratio dependence. We show the median and NMAD of the corrected Fe II/Mg II ratios for each sample in the bottom panel of Figure 6, and compare their distributions at redshift from $z = 0$ to $z > 7$. We analyze the evolutionary trend of Fe II/Mg II using both original Fe II/Mg II measurements and corrected values $(\mathrm{Fe\ II/Mg\ II})_c$ from our SDSS, XQ-100, and E-XQR-30 samples. The linear regression shows the slopes of Fe II/Mg II versus redshift are 0.035 ± 0.034 dex and 0.021 ± 0.041 dex in the logarithmic scale, respectively. Both slopes are consistent with zero within 1σ.

The median flux ratios before and after the Eddington ratio correction for the E-XQR-30, XQ-100, and SDSS samples are presented in Table 4. We find no significant redshift evolution in the corrected Fe II/Mg II flux ratios from $z = 0.95$ to 6.59,

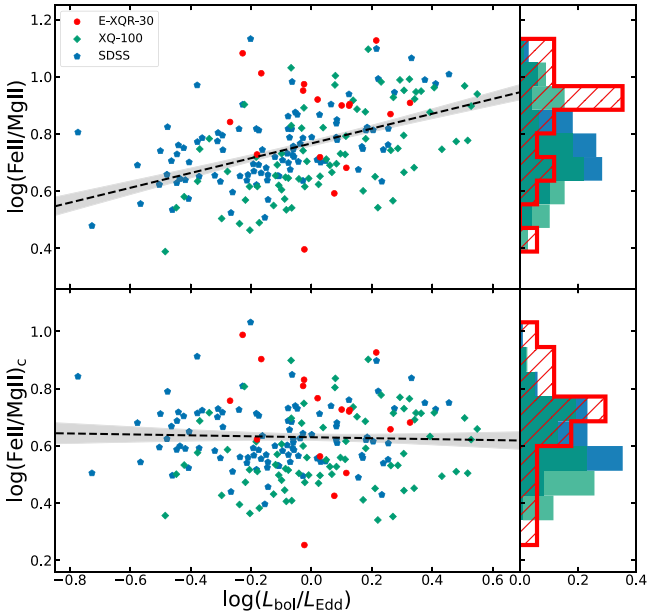

Figure 5. Correlation between the Eddington ratio and Fe II/Mg II line flux ratio. The upper panel shows the observed correlation and the lower panel shows the correlation after correcting for the dependence of the Eddington ratio (Section 4.2). The symbols and colors are the same as in Figure. 4. The side panels show the normalized histograms. The dashed lines are the linear regressions of the shown data points, and the results are $\log(\mathrm{Fe\ II/Mg\ II}) = 0.26 \times \log(L_{\rm bol}/L_{\rm Edd}) + 0.77$ in the upper panel and $\log(\mathrm{Fe\ II/Mg\ II})_c = -0.02 \times \log(L_{\rm bol}/L_{\rm Edd}) + 0.64$ in the lower panel. The uncertainty ranges of the linear regressions are obtained by the least-square method, and shown as the shaded regions. The weak negative slope of corrected Fe II/Mg II in the lower panel is insignificant.

suggesting early iron enrichment in the vicinity of massive black holes. Most measurements in the literature also fall within the 1σ range of the low-redshift SDSS sample. Possible systematic biases in these measurements will be discussed in Section 5.1. The large scatter of Fe II/Mg II flux ratios in the high-redshift sample will be discussed in Section 5.3.

We also estimate the dependence of the EWs of Fe II and Mg II on redshift using our three samples. With the linear regression, we calculate the slopes of the relations between EW and redshift for the two emission lines. The results in the logarithmic scale are 0.027 ± 0.065 and 0.011 ± 0.045, respectively, suggesting no significant evolution within 1σ.

5. Discussion

5.1. Systematic Uncertainties of the Fe II/Mg II Measurements

Systematic uncertainties of the Fe II/Mg II line ratio measurements were not included in the reported uncertainties. They can be caused by different iron templates, spectral fitting windows, emission-line fitting models, data reduction, etc. In this section, we discuss some systematic uncertainties of the measurements and their implications. We mostly focus on $(\mathrm{Fe\ II/Mg\ II})_c$, which is the measured Fe II/Mg II corrected for the Eddington ratio dependence using the method in Section 4.2.

First of all, the Fe II/Mg II measurements rely on iron templates. Our study used the T06 iron template. To test the systematic bias between the T06 and VW01 iron templates, we perform the same fitting method for three good E-XQR-30 spectra using the VW01 template and show the comparison in Table 5. Compared with the results from the T06 template, the

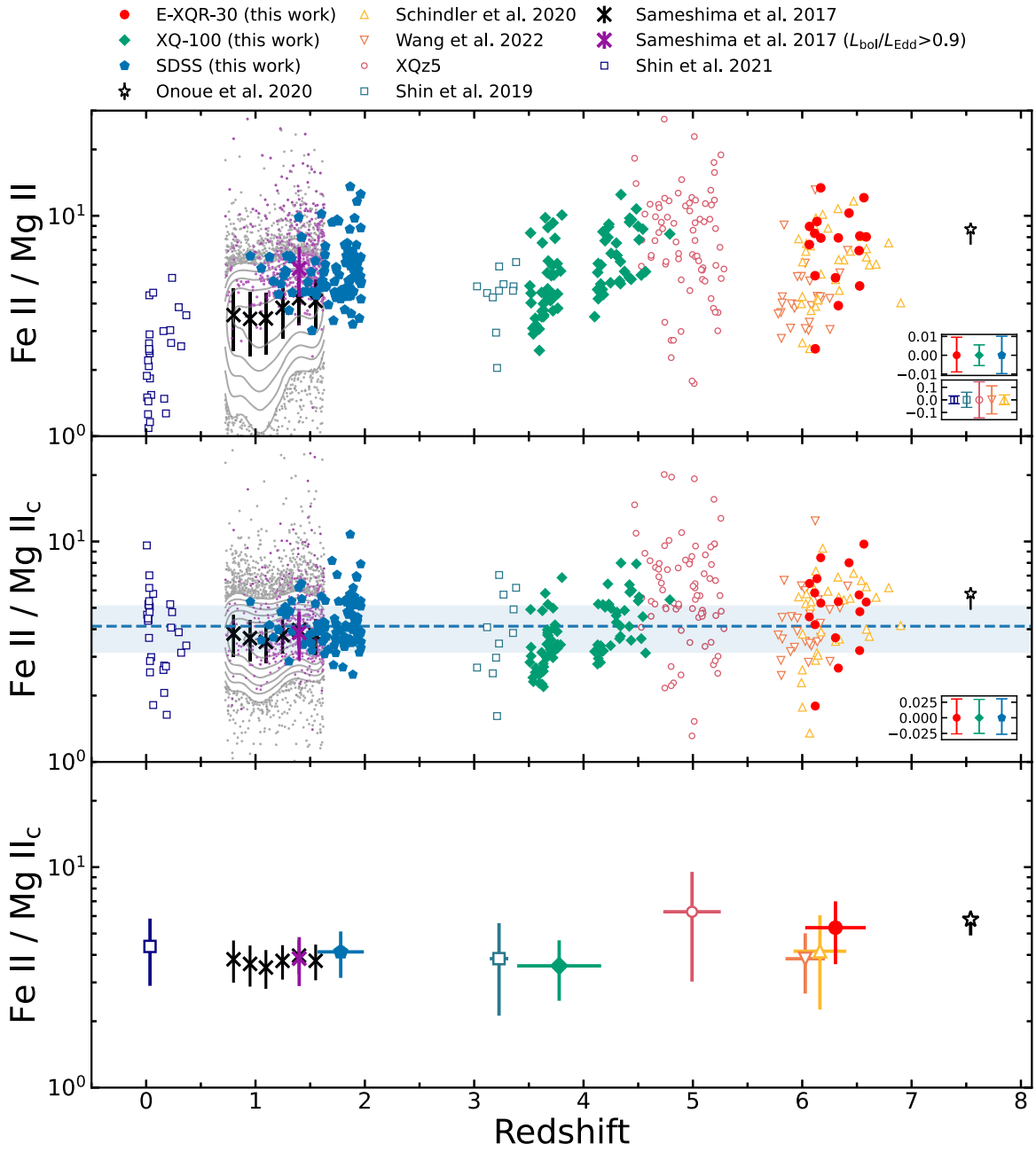

Figure 6. Fe II/Mg II line flux ratios at redshift from $z = 0$ to 7. The top panel shows the observed flux ratios. The middle panel shows the same ratios after correcting the Eddington ratio dependence (see details in Section 4.2). The bottom panel shows the median and $\pm1\sigma$ scatter of each sample. The filled symbols show the samples analyzed in this work (red: E-XQR-30, green: XQ-100, blue: low-redshift SDSS), and the open symbols show the samples in the literature. The different colors and symbols are described in the legend on the top. The subpanels in the lower right corners of the top and middle panels show the typical measurement errors in the logarithmic scale. The gray contours (with a step of 0.2 dex in the logarithmic scale) and gray dots represent the low-redshift sample of H. Sameshima et al. (2017). Their median Fe II/Mg II flux ratios at six redshift bins (a step of $\Delta z = 0.15$) are shown as the black crosses. Those with Eddington ratios over 0.9 are shown as the purple dots, and the median of this subsample is shown as the purple cross. The dashed line and its shaded region are the median value of the SDSS sample and its $\pm1\sigma$ range as our baseline at low redshift. The figure shows no apparent evolution of the line flux ratio with redshift.

Table 4
Fe II/Mg II Line Ratios of the Three Main Samples

Sample	Redshift	Fe II/Mg II	(Fe II/Mg II)$_c$
SDSS	0.95–1.97	5.56 ± 1.50	4.13 ± 0.98
XQ-100	3.51–4.79	5.30 ± 1.94	3.57 ± 1.09
E-XQR-30	6.05–6.59	7.94 ± 2.19	5.31 ± 1.68

Note. The redshifts are based on the Mg II emission-line measurements. For each sample, we show the median value and NMAD as the uncertainty.

Fe II/Mg II line ratios based on the VW01 template are lower by 33% at a 4σ significance. This is consistent with the results in the literature (e.g., J.-H. Woo et al. 2018; J. Shin et al. 2019; M. Onoue et al. 2020; J.-T. Schindler et al. 2020). The (Fe II/Mg II)$_c$ values are lower by 28% at a 2σ significance.

In addition, different fitting windows introduce systemic uncertainties of the measurements. The fitting windows used in our study are 2100–2750 Å and 2850–3100 Å for the continuum+iron fitting and 2750–2850 Å for the Mg II fitting, while H. Sameshima et al. (2017) used 2200–2700 Å and

Table 5
Examples of the Fe II/Mg II and Eddington Ratio Results Using the T06 and VW01 Iron Templates

Name	Fe II/Mg II		L_{bol}/L_{Edd}		(Fe II/Mg II)$_c$	
	T06	VW01	T06	VW01	T06	VW01
SDSS J0842+1218	$8.95^{+0.11}_{-0.10}$	$5.72^{+0.06}_{-0.05}$	$0.94^{+0.22}_{-0.22}$	$0.68^{+0.16}_{-0.14}$	$6.45^{+0.42}_{-0.35}$	$4.45^{+0.27}_{-0.23}$
PSO J158-14	$7.41^{+0.13}_{-0.12}$	$5.60^{+0.09}_{-0.08}$	$1.83^{+0.44}_{-0.42}$	$1.41^{+0.35}_{-0.37}$	$4.55^{+0.33}_{-0.26}$	$3.66^{+0.26}_{-0.22}$
PSO J239-07	$8.33^{+0.09}_{-0.09}$	$5.23^{+0.05}_{-0.06}$	$1.05^{+0.27}_{-0.24}$	$0.76^{+0.21}_{-0.17}$	$5.84^{+0.42}_{-0.31}$	$3.97^{+0.26}_{-0.23}$
Average	8.23 ± 0.63	5.51 ± 0.21	1.27 ± 0.40	0.95 ± 0.32	5.61 ± 0.79	4.03 ± 0.32

Note. Each property shows the results measured by both T06 and VW01 iron templates. The last row shows the average and standard deviation of the three quasars results.

2900–3500 Å for the continuum+iron fitting and 2700–2900 Å for the Mg II fitting. In order to check the influence of different fitting windows, we perform the following tests using the SDSS DR16 quasar spectra. We randomly select ∼500 spectra and ensure that the rest-frame 2100–3100 Å and 2200–3500 Å spectra of this sample are available. We then fit our model to this sample in the above two different types of fitting windows. The results show that the continuum and the Fe II and Mg II line flux measurements are all affected. The Fe II/Mg II flux ratios measured using our fitting windows are larger than those using the H. Sameshima et al. (2017) fitting windows by ∼15% at a 0.65σ significance.

Furthermore, different fitting models may affect the Fe II/Mg II measurements. For example our Fe II/Mg II measurements of the XQ-100 quasars are about 30% larger overall than the S. Lai et al. (2023) results at 1σ significance. We and S. Lai et al. (2023) both measured the XQ-100 sample, but using slightly different fitting methods. We used a single-component Gaussian model to fit the Mg II emission line, while S. Lai et al. (2023) used a multicomponent Gaussian model. We compare the median Fe II/Mg II values measured in both works and estimate the systematic bias introduced by the different models. We find a systematic difference of 30%. This is because the multicomponent model includes a wider component for Mg II, and thus provides a lower Fe II/Mg II value. This is also mentioned in J. Shin et al. (2021). When we compare the two results in Figure 6, we have applied a correction to the XQz5 sample to take into account the above systematic difference.

Finally, the spectra of the same quasar observed by different instruments or reduced by different pipelines can be inconsistent and introduce biases. We check quasars in common in different samples or studies. SDSS J0842+1218 and PSO J060+24 in our E-XQR-30 sample were included by S. Wang et al. (2022). We fit their GNIRS near-infrared spectra to calculate Fe II/Mg II using our fitting method. The calculated Fe II/Mg II values are smaller than our results by ∼45%. This difference is likely due to the low spectral resolution (R ∼600) of the GNIRS data (Y. Shen et al. 2019). We find that some peaks of the Fe II emission lines in the low-resolution spectra are smoothed, leading to a smaller value of the Fe II emission during the modeling process. Therefore, the Fe II/Mg II ratios are underestimated. This finding highlights the importance of a relatively high spectral resolution for the measurement of the Fe II/Mg II ratio.

5.2. Robustness of the Continuum Fitting

In this paper, our measurements are limited to a relatively short wavelength window compared to some previous studies of low-redshift quasars (e.g., M. Dietrich et al. 2003). We used the spectra of the XSHOOTER NIR arm, because one single power-law continuum cannot well characterize the entire wavelength range of the XSHOOTER VIS and NIR arms. The truncation at the short wavelength is chosen to be 2100 Å. This helps us avoid the flux calibration problem in the arm-connection range mentioned earlier and thus achieve a good model fit. The truncation at the long wavelength is at 3100 Å, which is limited by the effective wavelength coverage of the E-XQR-30 and XQ-100 spectra. In this case, our wavelength window does not cover the Balmer continuum edge $\lambda_{BE} = 3646$ Å, so we have used a fixed Balmer-to-power-law ratio (i.e., F_{BE}/F_{PL}). In this subsection, we address how our Fe II/Mg II measurements were affected by the truncated wavelength windows.

From the SDSS DR16 quasar sample, we select ∼200 spectra that cover the following wavelength windows: $\lambda_{rest} =$ 2100–2750 Å, 2850–3600 Å, 4180–4230 Å and 4440–4460 Å. The last two windows are the two reddest ranges in the SDSS spectra that are dominated by the continuum emission without broad-line emission. We perform our spectral fitting method to our truncated wavelength windows and to the new longer windows. The Balmer-to-power-law ratio is fixed to be 0.3. An example of SDSS quasar spectrum with both fitted models is presented in Appendix B. Figure 7 shows the comparison of the measured power-law slopes and Fe II/Mg II ratios between the two different window ranges. The median slope value (with its NMAD) is -1.55 ± 0.49 from our truncated wavelength windows, and is -1.62 ± 0.44 from the longer wavelength windows. The difference is less than 5%, suggesting that our truncated wavelength range works reasonably well. The Fe II/Mg II ratios are lower when the longer wavelength windows are used, and the difference is 20% at a $<1\sigma$ significance. We emphasize that this difference does not affect our results, since we use the same truncated wavelength range for all quasars in this study.

We further test the impact of the relative strength of the Balmer continuum using a series of Balmer-to-power-law ratios: 0.1, 0.3, 0.5, 0.8, and 1. We perform our spectral fitting method to our truncated wavelength windows and to the new longer windows, as we did above. Note that the truncated windows do not cover the Balmer edge $\lambda_{BE} = 3646$ Å. For the truncated windows, we fixed the Balmer-to-power-law ratio to be 0.3 earlier. Now we find that different ratios give similar Fe II/Mg II measurements within 1σ errors, which is consistent with the literature results (e.g., G. D. Rosa et al. 2011). For the longer fitting windows, a Balmer-to-power-law ratio of 0.1 or 0.3 gives the best fit. The best-fit Fe II/Mg II measurements are

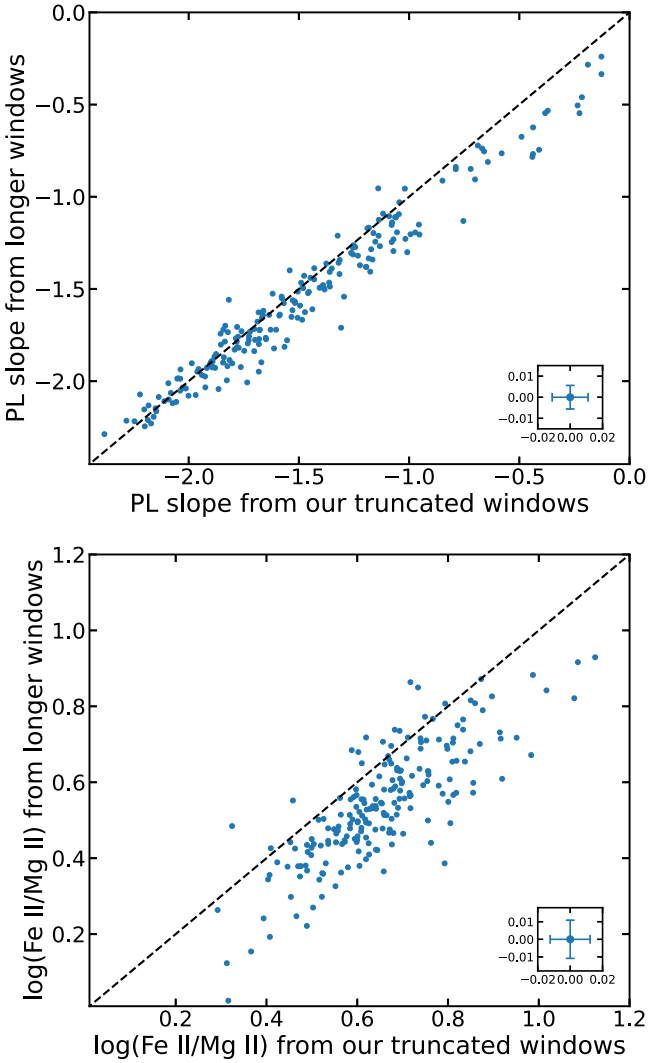

Figure 7. Comparison between our truncated wavelength windows and the longer wavelength windows. The upper and lower panels show the calculated power-law (PL) slopes and Fe II/Mg II, respectively. The blue symbols are the measurements of ∼200 SDSS DR16 quasars. The black dashed lines indicate the 1:1 reference line. The subpanel in the lower right corner of each panel shows the typical measurement errors. The Balmer-to-power-law ratio is fixed to be 0.3.

well consistent with those based on the truncated fitting windows. The longer fitting windows still lead to lower Fe II/Mg II measurements. The difference is only 10% at a 0.6σ significance. Therefore, it is reasonable to fix the Balmer-to-power-law ratio to be 0.3 for our main samples.

The above tests show that the choice of our spectral fitting windows has not brought obvious systematic biases. Our Fe II/Mg II measurements are reliable compared to those based on longer wavelength windows.

5.3. Large Scatter of Fe II/Mg II in the High-redshift Sample

We find that the scatter of the Fe II/Mg II flux ratios for the E-XQR-30 sample is larger than those for the XQ-100 and SDSS samples, as shown in Table 4 and Figure 6. We have not fully understood the reason for the relatively large scatter at $z > 6$, but we have a couple of explanations, including physical and nonphysical reasons.

In our quasar selection procedure from the E-XQR-30 sample, we have removed quasars at $z < 6.05$ whose spectra are severely affected by the atmospheric absorption in the near-infrared. For the remaining quasars at $z > 6.05$, we visually checked their spectra and found that their emission-line profiles and best-fit models all look reliable. We particularly inspect two quasars with the maximum and minimum corrected Fe II/Mg II ratios in this sample, including PSO J231-20 ($(\mathrm{Fe\,II/Mg\,II})_c = 9.73^{+0.76}_{-0.49}$; $\log(L_{\rm bol}[\mathrm{erg\ s^{-1}}]) = 47.26$) and CFHQS J1509-1749 ($(\mathrm{Fe\,II/Mg\,II})_c = 1.79^{+0.17}_{-0.11}$; $\log(L_{\rm bol}[\mathrm{erg\ s^{-1}}]) = 47.34$), and find no apparent anomaly in their Mg II line profiles. However, we cannot rule out the possibility that some spectra (particularly at $z = 6.15$–6.20 and $z = 6.30$–6.40) could have been slightly affected by relatively weak atmospheric absorption at 2.00–2.02 μm and 2.05–2.08 μm.

The large scatter in the high-redshift sample can be attributed to a physical origin. Based on ULAS J1342+0928 at $z = 7.5$, Y. Yoshii et al. (2022) raised a possibility that pair-instability supernovae (PISNe) that emerge from metal-free Population-III stars can supply iron to the BLR cloud in some quasars at high redshift. When PISNe were present, this extra iron supplier may affect the Fe/α abundance ratio. We will further discuss the early iron enrichment in Section 5.4.

5.4. Iron Enrichment in the Early Universe

Our results confirm the lack of a redshift evolution in the quasar Fe II/Mg II line ratios at redshifts up to $z \sim 6.6$. Thanks to the high data quality of our three samples over a wide redshift range, our measurements provide one of the most robust results for this conclusion. The nonevolution is consistent with the lack of redshift evolution of the BLR metallicity derived from other tracers. Although we do not cover the higher redshift range, the nonevolution trend seems to hold up to $z = 7.54$ (M. Onoue et al. 2020; Y. Yoshii et al. 2022). The age of the Universe was only 0.8 Gyr at $z \sim 6.6$, which is younger than the expected timescale of an efficient iron production by SNe Ia.

The origin for the lack of the Fe II/Mg II evolution is still unclear, and some possible solutions have been proposed. The typical time delay between the iron enrichment caused by SNe Ia and SNe II is thought to be about 1 Gyr, but recent observational constraints suggest that the SNe Ia rate has a delay-time distribution (DTD) that has a power-law shape t^{-1} over $t \sim 0.1$–10 Gyr (D. Maoz & F. Mannucci 2012; D. Maoz et al. 2014; S. A. Rodney et al. 2014; D. Maoz & O. Graur 2017). Therefore, the cosmic time for the SNe Ia iron enrichment may be earlier and the timescale for the enrichment completion may be statistically shorter than the previous expectation. Many Fe/α evolution models based on SNe Ia DTD and core-collapse supernova (CCSNe) point to a decline in Fe/α at high redshift, but the fact that our Fe II/Mg II measurements remain consistent up to $z \sim 6.6$ does not support the predictions of these models (e.g., D. Maoz & O. Graur 2017; H. Sameshima et al. 2017; Y. Yoshii et al. 2022).

Meanwhile, PISNe are candidates with a significant contribution to the iron enrichment, which is produced by the explosion of Population-III stars as massive as 150–300 $M_\odot$ (H. Umeda & K. Nomoto 2002). The iron yield from one PISNe with 280 $M_\odot$ is about one hundred times of that from a SN Ia (Y. Yoshii et al. 2022). Recently, Q.-F. Xing et al. (2023) reported a chemical signature for the existence of PISNe from

stars more massive than 140 $M_{\odot}$, highlighting the possibility of the PISNe contribution. Many recent studies also proposed a possible explanation of a rapid iron enrichment by a top-heavy initial mass function (IMF) with a power-law index larger than the classic value, indicating massive CCSNe and PISNe (D. Toyouchi et al. 2022; M. Ali-Dib & D. N. C. Lin 2023; J. Huang et al. 2023; J.-M. Wang et al. 2023). More observations and future studies are needed to confirm these candidates.

6. Summary

We have analyzed a sample of high-luminosity quasar spectra at $z \sim 6.0$–6.6, focusing on the Fe II/Mg II line ratios. This high-redshift sample is from the enlarged XQR-30 project that provided high-quality spectra observed by the XSHOOTER spectrograph at VLT. To make a consistent comparison at different redshifts, we have also analyzed two lower-redshift quasar samples with the same method, including a sample of 78 quasars at $z \sim 3.5$–4.8 from the XQ-100 project observed by VLT XSHOOTER and a sample of 99 quasars at $z \sim 0.95$–1.97 selected from the SDSS DR16Q.

We have performed comprehensive analyses for these luminosity-matched samples and measured their Fe II/Mg II line ratios with a correction for the Eddington ratio dependence. With a wide redshift coverage and high-quality data, our measurements are very suitable to trace the cosmic evolution of Fe II/Mg II in a unbiased manner. Our results confirmed no significant redshift evolution in Fe II/Mg II at redshifts from $z \sim 1$ to 6.6, suggesting a rapid iron enrichment in the early epoch. The nonevolution of Fe II/Mg II can be explained by a time-dependent SNe Ia rate, a nonstandard SN population such as PISNe, or a population with a top-heavy IMF.

The results presented in this paper will motivate further observations of quasars at $z \gtrsim 7$. The first-year JWST observations have discovered a sizable amount of low-luminosity AGNs at high redshift (e.g., Y. Harikane et al. 2023; D. D. Kocevski et al. 2023; R. Maiolino et al. 2023; M. Onoue et al. 2023; H. Übler et al. 2023; J. Matthee et al. 2024). Follow-up spectroscopy of these new AGN with JWST or future large telescopes will provide an opportunity to identify active SMBHs residing in metal-poor systems. Future near-infrared wide-field surveys such as Euclid and Nancy Roman Space Telescope will provide $z \sim 7$–9 quasars in a similar luminosity range as those presented in this study (Euclid Collaboration et al. 2019; X. Fan et al. 2019b; W. L. Tee et al. 2023).

Acknowledgments

We acknowledge support from the National Key R&D Program of China (2022YFF0503401), the National Science Foundation of China (12225301, 12150410307), and the China Manned Space Project with No. CMS-CSST-2021-A05 and CMS-CSST-2021-A06. Y.Z. was supported by the National Science Foundation through award SOSPADA-029 from the NRAO and through grant AST-1751404. R.D. is supported by the Australian Research Council Centre of Excellence for All Sky Astrophysics in 3 Dimensions (ASTRO 3D), through project number CE170100013. E.P.F. is supported by the international Gemini Observatory, a program of NSF's NOIRLab, which is managed by the Association of Universities for Research in Astronomy (AURA) under a cooperative agreement with the National Science Foundation, on behalf of the Gemini partnership of Argentina, Brazil, Canada, Chile, the Republic of Korea, and the United States of America.

We thank H. Sameshima for providing us his Fe II/Mg II data on the SDSS DR7 quasars. We thank L. C. Ho for helpful comments and suggestions. The data presented in this paper are based on observations collected at the European Southern Observatory under ESO programs 1103.A-0817(A), 189.A-0424(A), and 189.A-0424(B).

Funding for the Sloan Digital Sky Survey IV has been provided by the Alfred P. Sloan Foundation, the U.S. Department of Energy Office of Science, and the Participating Institutions. SDSS-IV acknowledges support and resources from the Center for High Performance Computing at the University of Utah. The SDSS website is www.sdss4.org.

Facilities: VLT:Kueyen (UT2 X-Shooter), Sloan.

Software: Astropy (Astropy Collaboration et al. 2018), Numpy (C. R. Harris et al. 2020), Scipy (P. Virtanen et al. 2020), Matplotlib (J. D. Hunter 2007).

Appendix A
The Degraded E-XQR-30

We degraded the E-XQR-30 quasar spectra from their effective spectral resolution (V. D'Odorico et al. 2023) to the SDSS spectral resolution $R \sim 2000$. Figure 8 shows the comparison of the measured Fe II/Mg II values of the degraded and original spectra.

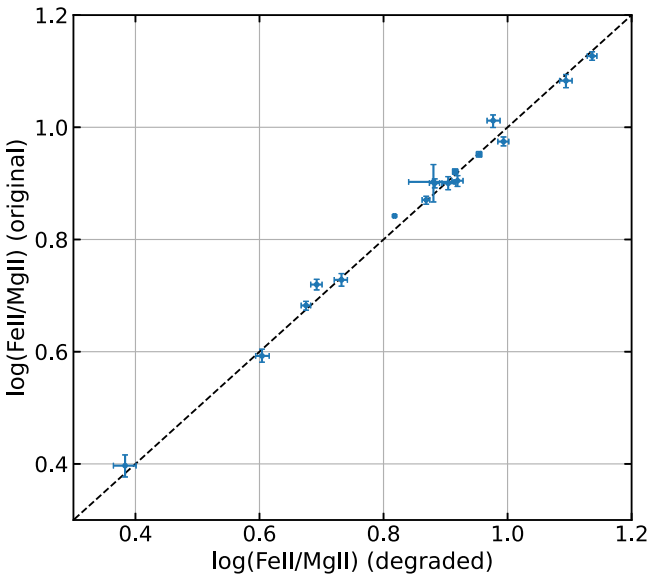

Figure 8. Comparison of the Fe II/Mg II line ratios between the degraded and original E-XQR-30 quasar spectra. The dashed line indicates the 1:1 reference line.

Appendix B
Effects of the Truncated Wavelength Windows on Spectral Fitting

Figure 9 shows the best-fit models of a SDSS spectrum fitted over our truncated wavelength windows and the longer windows, respectively. The Balmer-to-power-law ratio was fixed to be 0.3. The measured Fe II/Mg II line ratios are $3.06^{+0.23}_{-0.11}$ and $2.40^{+0.10}_{-0.14}$ respectively.

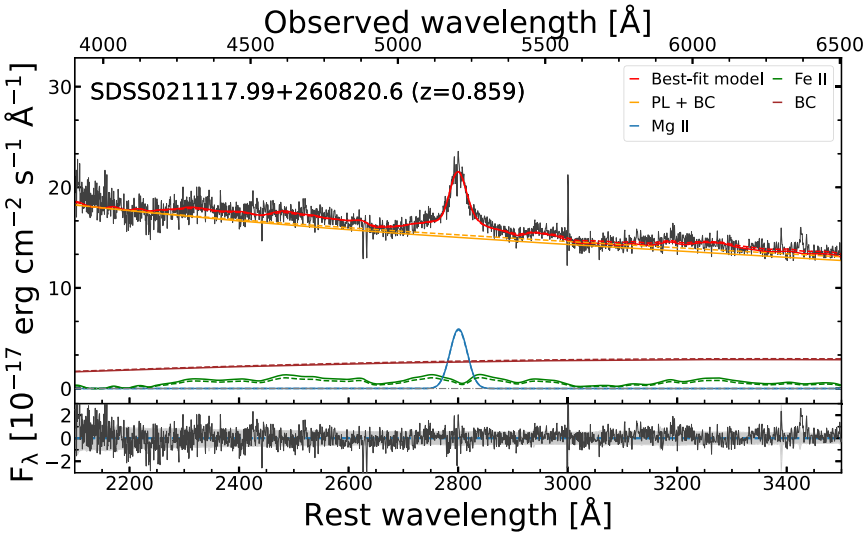

Figure 9. The color-coded lines have the same meaning as in Figure 3. The solid lines and dashed lines show the models fitted over our truncated wavelength windows and the longer windows, respectively. Since the best-fit models (red lines) are similar, we only display the residual flux of the best-fit model derived from our truncated wavelength windows in the lower subpanel.

ORCID iDs

Danyang Jiang https://orcid.org/0009-0003-6747-2221
Masafusa Onoue https://orcid.org/0000-0003-2984-6803
Linhua Jiang https://orcid.org/0000-0003-4176-6486
Samuel Lai https://orcid.org/0000-0001-9372-4611
Eduardo Bañados https://orcid.org/0000-0002-2931-7824
George D. Becker https://orcid.org/0000-0003-2344-263X
Manuela Bischetti https://orcid.org/0000-0002-4314-021X
Sarah E. I. Bosman https://orcid.org/0000-0001-8582-7012
Rebecca L. Davies https://orcid.org/0000-0002-3324-4824
Valentina D'Odorico https://orcid.org/0000-0003-3693-3091
Emanuele Paolo Farina https://orcid.org/0000-0002-6822-2254
Martin G. Haehnelt https://orcid.org/0000-0001-8443-2393
Chiara Mazzucchelli https://orcid.org/0000-0002-5941-5214
Jan-Torge Schindler https://orcid.org/0000-0002-4544-8242
Fabian Walter https://orcid.org/0000-0003-4793-7880
Yongda Zhu https://orcid.org/0000-0003-3307-7525

References

Aihara, H., Allende Prieto, C., An, D., et al. 2011, ApJS, 193, 29
Ali-Dib, M., & Lin, D. N. C. 2023, MNRAS, 526, 5824
Astropy Collaboration, Price-Whelan, A. M., Sipőcz, B. M., et al. 2018, AJ, 156, 123
Bañados, E., Venemans, B. P., Decarli, R., et al. 2016, ApJS, 227, 11
Bañados, E., Venemans, B. P., Mazzucchelli, C., et al. 2018, Natur, 553, 473
Barth, A. J., Martini, P., Nelson, C. H., & Ho, L. C. 2003, ApJ, 594, L95
Becker, G. D., Bolton, J. S., Madau, P., et al. 2015, MNRAS, 447, 3402
Becker, G. D., Pettini, M., Rafelski, M., et al. 2019, ApJ, 883, 163
Becker, G. D., Sargent, W. L. W., Rauch, M., & Carswell, R. F. 2012, ApJ, 744, 91
Bosman, S. E. I., Davies, F. B., Becker, G. D., et al. 2022, MNRAS, 514, 55
Bosman, S. E. I., Fan, X., Jiang, L., et al. 2018, MNRAS, 479, 1055
Carnall, A. C. 2017, arXiv:1705.05165
Cutri, R. M., Skrutskie, M. F., van Dyk, S., et al. 2003, 2MASS All Sky Catalog of Point Sources (Pasadena, CA: NASA/IPAC), http://irsa.ipac.caltech.edu/applications/Gator/
Dietrich, M., Appenzeller, I., Vestergaard, M., & Wagner, S. J. 2002, ApJ, 564, 581
Dietrich, M., Hamann, F., Appenzeller, I., & Vestergaard, M. 2003, ApJ, 596, 817
D'Odorico, V., Bañados, E., Becker, G. D., et al. 2023, MNRAS, 523, 1399
Dong, X.-B., Wang, J.-G., Ho, L. C., et al. 2011, ApJ, 736, 86
Dye, S., Lawrence, A., Read, M. A., et al. 2018, MNRAS, 473, 5113
Edge, A., Sutherland, W., Kuijken, K., et al. 2013, Msngr, 154, 32
Euclid Collaboration, Barnett, R., Warren, S. J., et al. 2019, A&A, 631, A85
Fan, X., Barth, A., Banados, E., et al. 2019b, BAAS, 51, 121
Fan, X., Narayanan, V. K., Lupton, R. H., et al. 2001, AJ, 122, 2833
Fan, X., Wang, F., Yang, J., et al. 2019a, ApJL, 870, L11
Farina, E. P., Schindler, J.-T., Walter, F., et al. 2022, ApJ, 941, 106
Freudling, W., Corbin, M. R., & Korista, K. T. 2003, ApJ, 587, L67
Grandi, S. A. 1982, ApJ, 255, 25
Greggio, L., & Renzini, A. 1983, A&A, 118, 217
Hamann, F., & Ferland, G. 1993, ApJ, 418, 11
Hamann, F., & Ferland, G. 1999, ARA&A, 37, 487
Hamann, F., Korista, K. T., Ferland, G. J., Warner, C., & Baldwin, J. 2002, ApJ, 564, 592
Harikane, Y., Zhang, Y., Nakajima, K., et al. 2023, ApJ, 959, 39
Harris, C. R., Millman, K. J., van der Walt, S. J., et al. 2020, Natur, 585, 357
Huang, J., Lin, D. N. C., & Shields, G. 2023, MNRAS, 525, 5702
Hunter, J. D. 2007, CSE, 9, 90
Iwamuro, F., Kimura, M., Eto, S., et al. 2004, ApJ, 614, 69
Iwamuro, F., Motohara, K., Maihara, T., et al. 2002, ApJ, 565, 63
Jiang, L., Fan, X., Vestergaard, M., et al. 2007, AJ, 134, 1150
Jiang, L., McGreer, I. D., Fan, X., et al. 2016, ApJ, 833, 222
Jones, A., Noll, S., Kausch, W., Szyszka, C., & Kimeswenger, S. 2013, A&A, 560, A91
Juarez, Y., Maiolino, R., Mujica, R., et al. 2009, A&A, 494, L25
Kawara, K., Murayama, T., Taniguchi, Y., & Arimoto, N. 1996, ApJ, 470, L85
Kocevski, D. D., Onoue, M., Inayoshi, K., et al. 2023, ApJL, 954, L4
Kurk, J. D., Walter, F., Fan, X., et al. 2007, ApJ, 669, 32
Lai, S., Bian, F., Onken, C. A., et al. 2022, MNRAS, 513, 1801
Lai, S., Onken, C. A., Wolf, C., et al. 2023, MNRAS, 526, 3230
Lai, S., Onken, C. A., Wolf, C., Bian, F., & Fan, X. 2024, MNRAS, 527, 3912
Lawrence, A., Warren, S. J., Almaini, O., et al. 2007, MNRAS, 379, 1599
López, S., D'Odorico, V., Ellison, S. L., et al. 2016, A&A, 594, A91
Lyke, B. W., Higley, A. N., McLane, J. N., et al. 2020, ApJS, 250, 8
Maiolino, R., Juarez, Y., Mujica, R., Nagar, N. M., & Oliva, E. 2003, ApJ, 596, L155
Maiolino, R., Scholtz, J., Curtis-Lake, E., et al. 2023, arXiv:2308.01230
Maoz, D., & Graur, O. 2017, ApJ, 848, 25
Maoz, D., & Mannucci, F. 2012, PASA, 29, 447
Maoz, D., Mannucci, F., & Nelemans, G. 2014, ARA&A, 52, 107
Matsuoka, Y., Iwasawa, K., Onoue, M., et al. 2018, ApJS, 237, 5
Matsuoka, Y., Iwasawa, K., Onoue, M., et al. 2022, ApJS, 259, 18
Matthee, J., Naidu, R. P., Brammer, G., et al. 2024, ApJ, 963, 129
Mazzucchelli, C., Bañados, E., Venemans, B. P., et al. 2017, ApJ, 849, 91
Mazzucchelli, C., Bischetti, M., D'Odorico, V., et al. 2023, A&A, 676, A71

McMahon, R. G., Banerji, M., Gonzalez, E., et al. 2013, Msngr, 154, 35
Nagao, T., Marconi, A., & Maiolino, R. 2006, A&A, 447, 157
Noll, S., Kausch, W., Barden, M., et al. 2012, A&A, 543, A92
Onoue, M., Bañados, E., Mazzucchelli, C., et al. 2020, ApJ, 898, 105
Onoue, M., Inayoshi, K., Ding, X., et al. 2023, ApJL, 942, L17
Reed, S. L., McMahon, R. G., Banerji, M., et al. 2015, MNRAS, 454, 3952
Richards, G. T., Lacy, M., Storrie-Lombardi, L. J., et al. 2006, ApJS, 166, 470
Rodney, S. A., Riess, A. G., Strolger, L.-G., et al. 2014, AJ, 148, 13
Rosa, G. D., Decarli, R., Walter, F., et al. 2011, ApJ, 739, 56
Rosa, G. D., Venemans, B. P., Decarli, R., et al. 2014, ApJ, 790, 145
Ross, N. P., & Cross, N. J. G. 2020, MNRAS, 494, 789
Sameshima, H., Yoshii, Y., & Kawara, K. 2017, ApJ, 834, 203
Sameshima, H., Yoshii, Y., Matsunaga, N., et al. 2020, ApJ, 904, 162
Schindler, J.-T., Farina, E. P., Banados, E., et al. 2020, ApJ, 905, 51
Schlegel, D. J., Finkbeiner, D. P., & Davis, M. 1998, ApJ, 500, 525
Shen, Y., Greene, J. E., Strauss, M. A., Richards, G. T., & Schneider, D. P. 2008, ApJ, 680, 169
Shen, Y., Wu, J., Jiang, L., et al. 2019, ApJ, 873, 35
Shin, J., Nagao, T., Woo, J.-H., & Le, H. A. N. 2019, ApJ, 874, 22
Shin, J., Woo, J.-H., Nagao, T., Kim, M., & Bahk, H. 2021, ApJ, 917, 107
Tang, J.-J., Goto, T., Ohyama, Y., et al. 2019, MNRAS, 484, 2575
Tee, W. L., Fan, X., Wang, F., et al. 2023, ApJ, 956, 52
Temple, M. J., Ferland, G. J., Rankine, A. L., Chatzikos, M., & Hewett, P. C. 2021, MNRAS, 505, 3247
Thompson, K. L., Hill, G. J., & Elston, R. 1999, ApJ, 515, 487
Toyouchi, D., Inayoshi, K., Ishigaki, M. N., & Tominaga, N. 2022, MNRAS, 512, 2573
Tsuzuki, Y., Kawara, K., Yoshii, Y., et al. 2006, ApJ, 650, 57
Übler, H., Maiolino, R., Curtis-Lake, E., et al. 2023, A&A, 677, A145
Umeda, H., & Nomoto, K. 2002, ApJ, 565, 385
Venemans, B. P., Findlay, J. R., Sutherland, W. J., et al. 2013, ApJ, 779, 24
Vernet, J., Dekker, H., D'Odorico, S., et al. 2011, A&A, 536, A105
Vestergaard, M., & Osmer, P. S. 2009, ApJ, 699, 800
Virtanen, P., Gommers, R., Oliphant, T. E., et al. 2020, NatMe, 17, 261
Wang, F., Yang, J., Fan, X., et al. 2019, ApJ, 884, 30
Wang, F., Yang, J., Fan, X., et al. 2021, ApJL, 907, L1
Wang, J.-M., Zhai, S., Li, Y.-R., et al. 2023, ApJ, 954, 84
Wang, S., Jiang, L., Shen, Y., et al. 2022, ApJ, 925, 121
Willott, C. J., Delorme, P., Reylé, C., et al. 2010, AJ, 139, 906
Woo, J.-H., Le, H. A. N., Karouzos, M., et al. 2018, ApJ, 859, 138
Woosley, S. E., & Hoffman, R. D. 1992, ApJ, 395, 202
Wu, X.-B., Wang, F., Fan, X., et al. 2015, Natur, 518, 512
Xing, Q.-F., Zhao, G., Liu, Z.-W., et al. 2023, Natur, 1, 712
Yang, J., Wang, F., Fan, X., et al. 2021, ApJ, 923, 262
Yoshii, Y., Sameshima, H., Tsujimoto, T., et al. 2022, ApJ, 937, 61
Yoshii, Y., Tsujimoto, T., & Kawara, K. 1998, ApJ, 507, L113